

THESIS APPROVED BY

---

Date

---

[Edward Goldobin], Ph.D.

HIGH EFFICIENCY JOSEPHSON RATCHET  
BASED ON YBCO JJ FABRICATED WITH A  
FOCUSED HE-ION BEAM

---

by

**Alireza Jozani**

---

Physikalische Institut–Experimentalphysik II, University of Tübingen,  
Auf der Morgenstelle 14, 72076, Germany.

---

Jun, 2023

# Acknowledgments

Thank you, Thank you, Thank you, thank you, Thank you, Thank you.

*To my beloved parents*

# Contents

<b>Contents</b>	<b>2</b>
<b>Acknowledgments</b>	<b>iii</b>
<b>1 Introduction</b>	<b>1</b>
1.1 Josephson Junction	3
1.2 Current Voltage Characteristic ( <i>I-V</i> )	8
1.3 Josephson Junction in a Magnetic Field	10
<b>2 Theory of Ratchet</b>	<b>13</b>
2.1 An Overview of Josephson Ratchet	13
2.1.1 Josephson Ratchet Operation	16
2.1.2 Efficiency	20
2.1.3 Theoretical Design of JJ with In-line Geometry	22
<b>3 Fabrication and Implementation</b>	<b>27</b>
3.1 Sample Information	27
3.2 Sample Layout	28
3.3 Sample Fabrication	28
3.4 He-FIB	30
3.5 Characterization	34
3.6 Implementation of an In-line Geometry Josephson Ratchet	37

<b>4 Experimental Results</b>	<b>39</b>
4.1 An Overview	39
4.2 Ratchet A22	39
4.2.1 Experimental Simulation of A22	49
4.3 Ratchet A15	51
4.4 Driving the Ratchet with a Stochastic Signal	56
4.4.1 External noise	57
4.4.2 Internal noise	59
4.5 Conclusion	62

# List of Tables

3.1	The maximum $I_c$ is determined by measuring $I_c(H)$ and selecting the highest value, which may be reduced at $I_{coil} \neq 0$ .	34
3.2	Comparison table of target parameters between ratchet A15 and A22.	38
4.1	Comparison table of target and actual parameters of ratchet A22.	40
4.2	Comparison table of target and actual parameters of ratchet A15	51

# List of Figures

1.1	A JJ made by the barrier potential insulator which was made by two close superconductors left and right.	3
1.2	Schematic electronic equivalent circuit of JJ and a RCSJ.	6
1.3	Plots of tilted washboard potential $U(\varphi)$ for several values of the tilt (bias current) $\gamma$ . Phase-particle, trapped in the minimum at $\gamma < 1$ escapes from the minimum when $\gamma \geq 1$ and slides down the potential.	7
1.4	Current Voltage Characteristic, IVC of a symmetric potential.	9
1.5	Negative and positive $I_c(\Phi_J)$ are symmetric for fixed $\Phi_J$ . For example, here for the fixed value of $\Phi_J/\Phi_0 = 44.5$ we observe, $ I_{c+}/I_0  =  I_{c-}/I_0  = 0.75$ .	12
2.1	(a) An example of a particle trapped in a schematic asymmetric potential (b) indicates schematically meaning of asymmetric.	14
2.2	Schematic example of a non-hysteretic IVC for an asymmetric Josephson potential. $I_{c+}$ is positive critical current and $I_{c-}$ is negative critical current.	15
2.3	A rectification curve represents an averaged velocity of a particle ( $\langle \dot{\varphi} \rangle \propto V$ ) as a function of an applied ac-drive amplitude $I_{ac}$ . The interval between $I_{c+}$ and $I_{c-}$ is called operation interval or the rectification window. Its size is defined as $\Delta \equiv I_{c-} - I_{c+}$ .	16
2.4	A ratchet potential for $I_{dc} = 0, I_{c-}, I_{c+}$ .	18
2.5	The schematic loaded ratchet up to countercurrent $ I_{dc}  = 0.2 \mu\text{A}$ .	19

2.6	(a) Asymmetric IVC with $\mathcal{A} = 4$ . (b) The rectification curves for several values of $I_{dc}$ .	20
2.7	(c) Average input ac power $\bar{P}_{in}$ , (d) average output dc power $\bar{P}_{out}$ , (e) efficiency $\eta$ .	21
2.8	(a) The in-line geometry of a (JJ) consists of superconducting where the dashed line representing the barrier JJ surrounded with superconductors. (b) C The critical density $j_c$ as a function of distance $x$ .	22
2.9	Asymmetric $I_c(f)$ , which is obtained by simulation of solution of eq. (2.3).	24
2.10	(a) Asymmetry parameter $\mathcal{A}$ vs. magnetic flux $f$ for different values of $f^M$ ; (b) asymmetry parameter $\mathcal{A}$ vs. strength of in-line geometry $f^M$ .	25
3.1	YBCO film on 2 inch LSAT wafer. (a) The picture of scanning electron microscope of the surface of the sample. The critical temperature $T_c$ , the value of the current density $j_c$ , and the other info are provided by Ceraco. (b) A schematic picture of the chip with its different layer deposition	27
3.2	Layout of the small chip. The hatched light green areas correspond to the Au covered pads and the blue is the LSAT substrate, the guide lines are also covered by Au, and on the bridges Au is removed down to YBCO.	28

3.3	Mask used during the patterned process. (a) Mask used during step (i) for the etching of gold. The blue zone is where the gold has been removed and only YBCO remains. The yellow zones belong to where the gold still remains. (b) The mask used during step (ii) for the etching of YBCO. The areas in blue represent the regions where the YBCO still remains. The black area represents LSAT (substrate). Note that in the regions where the gold remains from the first step (for example, over the pads), has not been removed during the second step.	30
3.4	The microscope pictures of the sample after each step of the lithography process. (a) Picture of the pads after the first step. The dark areas are YBCO and the yellow areas are gold. (b) The picture of the bridges after the second step. The yellow area is gold, the dark area is LSAT, the blue area is YBCO where the junction will be finally irradiated and the purple lines are guide lines for our next step HIM	30
3.5	The poster of He-FIB.	32
3.6	(a) Red line indicates focused He ion beam on atomic level with the width of the order of few nm order (b) Schematic sketch of the barrier JJ produced by He-FIB, the green line indicates the barrier JJ.	33
3.7	BJJs characterization $j_c(D)$ experimental data and fit. 12 BJJ's with the dose $D = 450\ldots700$ ion/nm. The width of the BJJ's is 2.8 $\mu\text{m}$ and the film thickness is 30 nm.	35
3.8	IVC and $I_c(H)$ of junction B28 with dose 350 ion/nm.	35
3.9	IVC and $I_c(H)$ of junction D19 with dose 450 ion/nm.	36
3.10	IVC and $I_c(H)$ of junction D22 with dose 505 ion/nm.	36
3.11	IVC and $I_c(H)$ of junction B33 with dose 600 ion/nm.	36

- 3.12 Sketch of a ratchet. The blue zone is YBCO, the red solid lines are the resistive wall, dash red line is the BJJ and arrows show the flow of the supercurrent. 37
- 4.1 IVC of the ratchet A22 at  $I_{\text{coil}} = 0$  where  $|I_{c+}| \approx |I_{c-}| \approx 8.43 \mu\text{A}$ . 41
- 4.2 Critical current versus magnetic coil current of the ratchet A22. We used a voltage criterion equal to  $1 \mu\text{V}$  for this measurement. 42
- 4.3 Value of asymmetry parameter, which shows the maximum asymmetry, is  $\mathcal{A} \approx 7$  at the value of  $I_{\text{coil}} = -69 \text{ mA}$ . 43
- 4.4 IVC of the ratchet A22 at the optimum magnetic field (coil current)  $I_{\text{coil}} = -69 \text{ mA}$  exhibits  $|I_{c+}| \approx 1.53 \mu\text{A}$  and  $|I_{c-}| \approx -13.8 \mu\text{A}$  that makes  $\mathcal{A} \approx 7$ . 44
- 4.5 The rectification curve for the ratchet A22 at  $I_{\text{coil}} = -69 \text{ mA}$  where  $|I_{c-}| \approx 15.2 \mu\text{A}$ ,  $|I_{c+}| \approx 2.2 \mu\text{A}$  and RW  $\Delta \approx 13 \mu\text{A}$ . 45
- 4.6 The rectification curve for the ratchet A22 at  $I_{\text{coil}} = -69 \text{ mA}$  for several  $I_{\text{dc}}$  up to  $|I_{\text{dc}}| = 5 \mu\text{A}$ . 46
- 4.7 (a)  $\overline{P_{\text{in}}}$ , (b)  $\overline{P_{\text{out}}}$ , (c) efficiency  $\eta$ . 47
- 4.8 Simulations (lines) versus the experimental data (dots) of  $\overline{V}_{\text{dc}}(I(t))$  49
- 4.9 Simulations (lines) versus the experimental data (dots) of (a)  $\overline{P_{\text{in}}}$ , (b)  $\overline{P_{\text{out}}}$ , and (c)  $\eta$ . 50
- 4.10 IVC of the ratchet A15 at  $I_{\text{coil}} = 0$ .  $|I_{c+}| = |I_{c-}| \approx 21 \mu\text{A}$  and  $R_N \approx 32 \Omega$ . 52
- 4.11 Critical current versus magnetic coil current of the ratchet A15 52
- 4.12 The value of asymmetry parameter which shows the maximum asymmetry  $\mathcal{A} \approx 7$  at optimum magnetic  $I_{\text{coil}} = 75 \text{ mA}$ . 53
- 4.13 An asymmetric IVC of the ratchet A15 at the optimum  $I_{\text{coil}} = 75 \text{ mA}$  has  $|I_{c-}| \approx 24.5 \mu\text{A}$  and  $|I_{c+}| \approx 3.5 \mu\text{A}$ . 53
- 4.14 The rectification curve for the ratchet A15 at  $I_{\text{coil}} = 75 \text{ mA}$ . 54

4.15 The rectification curve for the ratchet A15 at $I_{\text{coil}} = 75 \text{ mA}$ for several $I_{\text{dc}}$ up to $ I_{\text{dc}}  = 8.92 \mu\text{A}$ .	54
4.16 (a) $\overline{P_{\text{in}}}$ , (b) $\overline{P_{\text{out}}}$ , (c) efficiency $\eta$	55
4.17 (a) The Gaussian distribution of random signal with the width $\sigma$ (b) The random signal depends on time.	56
4.18 Simulation of $\overline{V}_{\text{dc}}$ drive with Gaussian signal.	57
4.19 (a) $\overline{P_{\text{in}}}$ , (b) $\overline{P_{\text{out}}}$ , (c) and $\eta$	58
4.20 IVC of A15 at $T \approx 4.2 \text{ K}$ and $35 \text{ K}$ at zero magnetic field $I_{\text{coil}} = 0$ .	60
4.21 IVC for the ratchet A15 at around temperature $35 \text{ K}$ for the two values of $I_{\text{coil}}$ : zero and the optimum magnetic field.	61
4.22	62

# Chapter 1

## Introduction

Typically, when referring to a ratchet or Brownian motion, one can envision a system characterized by weak interaction with a surrounding large bath. In such a system, the periodic symmetric nature of the potential is broken, and an asymmetric potential would be immediately substituted/subjected/suggested to describe the ratchet (e.g., see the schematic fig. 2.1). It has been demonstrated that in this type of system, where a particle is trapped in an asymmetric potential with directed transport, it leads to a system highly in the out of equilibrium state where useful work can be performed by the particle under certain conditions. One significant effect in such a non-equilibrium state is the dominance of time-dependent perturbations, which consequently leads to a non-negligible influence of thermal noise. [1] These effects can be captured and studied.

This master's thesis work focuses on the investigation of a High Temperature Superconductors (HTSs), namely YBCO, where a Josephson Ratchet was fabricated(designed) using a Helium focused ion Beam (He-FIB) technique. The Josephson ratchet is implemented by an in-line geometry of Josephson junction (see e.g. fig. 2.8(a)) by He-FIB. The Josephson ratchet was experimentally driven in both deterministic and stochastic regimes. We record and achieve a significantly high efficient Josephson

ratchet. Subsequently, we explored the effects of external and thermal (internal) noise, particularly emphasizing the dominance of time-dependent perturbations. [1] The thesis is organized as follows:

**In Chapter 1** we delve into the concept of Josephson effect with  $2\pi$  gauge invariant phase periodic in the presence of magnetic field, focusing on a particle trapped in a symmetric potential.

**In Chapter. 2** we will first theoretically investigate how the particle trapped on an asymmetric Josephson potential can be operated to produce useful work with certain efficiency. [2] [3]. Next the normalized critical current across the ratchet device is numerically simulated under certain boundary conditions to obtain preliminary insights into the necessary design parameters for a Josephson ratchet.

**In Chapter 3**, we thoroughly investigate the lithography process for our sample and explore the irradiation techniques (He-FIB) employed to fabricate the Josephson ratchet. Subsequently, we report the characterization of our sample through experimental measurement of the critical current density.

**In Chapter 4**, we present the experimental results of two Josephson ratchet devices operating in different regimes: deterministic (i.e., when the system is driven with an AC-drive amplitude) and stochastic (i.e., when the Josephson ratchet is driven with a randomly varying signal following a Gaussian distribution). We report on parameters such as  $\bar{V}_{dc}$ ,  $\bar{P}_{out}$ ,  $\bar{P}_{in}$ , and the efficiency  $\eta$ . Furthermore, since we operate in a quasistatic regime, we can simulate all the ratchet parameters based on the current-voltage characteristics. Notably, we investigate how external noise affects the particle's dynamics in an asymmetric potential, enabling ratchet operation. Lastly, we explore the influence of thermal noise, modeled as a random signal following a Gaussian distribution. Finally, we conclude the work with a concise summary, discussing the applications, and providing an outlook on future research directions.

## 1.1 Josephson Junction

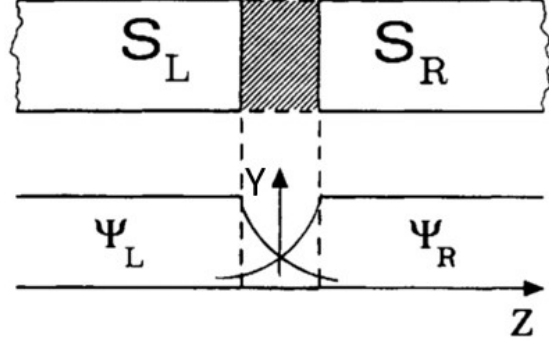


Figure 1.1: A JJ made by the barrier potential insulator which was made by two close superconductors left and right.

The Josephson effect is a phenomenon that describes the flow of supercurrent, which is a current without dissipation, between two separated superconductors. When two superconductors, denoted as  $S_L$  and  $S_R$ , are brought close together, with only a small gap and a barrier separating them, a continuous supercurrent flows between them. This device is known as a Josephson junction (JJ), as shown schematically in fig. 1.1. The left superconductor has a wave function of Cooper pairs (a pair of electrons or other fermions bound together at low temperatures)  $\psi_L(t, \mathbf{x}) = |\psi_0| e^{i\phi_L(t, \mathbf{x})} = \sqrt{n_{s,L}} e^{i\phi_L(t, \mathbf{x})}$ . Similarly, the wave function for the right superconductor,  $S_R$ , is given by  $\psi_R(t, \mathbf{x}) = |\psi_0| e^{i\phi_R(t, \mathbf{x})} = \sqrt{n_{s,R}} e^{i\phi_R(t, \mathbf{x})}$ . If the potential difference across the junction is  $V$ , then the potential energy difference between the two superconductors is  $2eV$ , since each Cooper pair has twice the charge of an electron. The Schrödinger equation for these two quantum states,  $\psi_L$  and  $\psi_R$ , is as follows

$$i\hbar \frac{\partial}{\partial t} \begin{pmatrix} \sqrt{n_{s,L}} e^{i\phi_L} \\ \sqrt{n_{s,R}} e^{i\phi_R} \end{pmatrix} = \begin{pmatrix} eV & K \\ K & -eV \end{pmatrix} \begin{pmatrix} \sqrt{n_{s,L}} e^{i\phi_L} \\ \sqrt{n_{s,R}} e^{i\phi_R} \end{pmatrix}, \quad (1.1)$$

where  $K$  is an interaction coupling constant that represents the strength of the interaction coupling between the wave functions of the two superconductors.  $n_{s,i}$  ( $i = L, R$ )

or  $R$ ) is the charge carrier density (Cooper pair density) which is proportional to the current  $I$  through the supercurrent density  $j_s = q_s \cdot n_s \cdot v_s$ , where  $v_s$  is the velocity vector of the Cooper pairs,  $q_s$  is the Cooper charge, and  $A_J$  is the surface area of the Josephson junction.

After taking the derivative of equation (1.1) and splitting the real and imaginary parts, we obtain the following set of equations for  $\phi_L, \phi_R, n_{s,L}$ , and  $n_{s,R}$  [4]

$$\begin{aligned}\dot{n}_{s,L} &= \frac{2K}{\hbar} \sqrt{n_{s,L} n_{s,R}} \sin(\phi_L - \phi_R), \\ \dot{n}_{s,R} &= -\frac{2K}{\hbar} \sqrt{n_{s,L} n_{s,R}} \sin(\phi_L - \phi_R),\end{aligned}\tag{1.2}$$

$$\begin{aligned}\dot{\phi}_L &= \frac{K}{\hbar} \sqrt{\frac{n_{s,L}}{n_{s,R}}} \cos(\phi_L - \phi_R) + \frac{eV}{\hbar}, \\ \dot{\phi}_R &= \frac{K}{\hbar} \sqrt{\frac{n_{s,L}}{n_{s,R}}} \cos(\phi_L - \phi_R) - \frac{eV}{\hbar}.\end{aligned}\tag{1.3}$$

The phase differences between two superconductors is defined  $\varphi_0 \equiv \phi_L - \phi_R$  (without presence of a magnetic field). Thus the differences of  $\dot{\varphi}_0 \equiv \dot{\phi}_L - \dot{\phi}_R$  yields the 2nd Josephson equation as follows

$$\frac{\partial \varphi_0(t, \mathbf{x})}{\partial t} = \frac{2eV(t)}{\hbar} = \frac{2\pi V}{\Phi_0},\tag{1.4}$$

where  $\Phi_0 = \frac{h}{2e} = 2.068 \times 10^{-15}$  Wb is magnetic flux quantum. Eq. (1.4) tells us about the linear evolution of phase differences across the junction for constant applied voltage. It immediately follows from eq. (1.4) that if there is no voltage across the junction i.e.,  $V = 0$  then  $\varphi_0$  is constant and this implies constant arguments of the angular functions in eq. (1.2) and so  $\dot{n}_{s,L} = -\dot{n}_{s,R}$ . Therefore i.e., if  $n_{s,L} = n_{s,R}$ , then  $n_{s,i} = \text{const}$  and so current should flow uniformly between the two superconductors, otherwise the superconductors would be charged and the supercurrent would flow non-uniformly. Thus, the supercurrent density depends on the phase difference  $j_s(\varphi_0)$  which has to be gauge invariant. That is, in the presence of the magnetic field, the

supercurrent density becomes as,  $j_s(\psi) = q_s \operatorname{Re} \left\{ \psi^* \left( \frac{\hbar}{mi} \vec{\nabla} - \frac{q_s}{m} \vec{A} \right) \psi \right\} = \frac{q_s n_s \hbar}{m_s} \vec{\nabla} \varphi$ <sup>1</sup>, where in the last equality we just insert the definition of Cooper pair wave functions and defined  $\vec{\nabla} \varphi := \vec{\nabla} \varphi_0 - \frac{2\pi}{\Phi_0} \vec{A}$  which is the gauge invariant phase differences in the presence of magnetic field<sup>2</sup>. Now if we integrate the supercurrent density over the area of BJJ, we will get  $\varphi(t, \mathbf{x}) = \varphi_0 - \frac{2\pi}{\Phi_0} \int_L^R A_y(\mathbf{x}) dx$  where  $A_y$  is a homogeneous magnetic vector potential in the direction of  $y$  axis, and  $\varphi$  is the gauge invariant phase differences across the JJ. Since  $\varphi$  is a gauge invariant phase, the direction of the magnetic field does not matter, however it must be perpendicular to the surface of the JJ. Now we notice that  $\varphi(t, \mathbf{x})$  inside the JJ is defined as modulo  $2\pi$  ( $\psi(t, \mathbf{x}) = \sqrt{n_s} e^{i(\varphi(t, \mathbf{x}) + 2\pi)} = \sqrt{n_s} e^{i\varphi(t, \mathbf{x})}$ ), and so phase changes by  $2n\pi$  ( $n$  is an integer) does not change the wave function  $\psi$  and, additionally,  $j_s(\varphi)$  is time reversal invariant ( $j_s(\varphi) = -j_s(-\varphi)$ ). These considerations together lead us to the definition of the uniform gauge invariant supercurrent density, which necessarily needs to be an odd,  $2\pi$  periodic function of the phase difference i.e.  $j_s(\varphi) = j_s(\varphi + 2n\pi)$ . Thus the 1st Josephson equation could be defined as follow

$$I_s := I_0 \sin [\varphi(t)]. \quad (1.5)$$

This is the supercurrent which flows uniformly between the two superconductors and is called Josephson supercurrent. In the eq. (1.5),  $I_0$  is the maximum supercurrent that can flow through JJ and is called the critical current. [6]

---

<sup>1</sup>The Schrödinger equation implies the continuity equation  $\left( \frac{\partial |\psi(t, x)|^2}{\partial t} = -\vec{\nabla} \cdot j(t, x) \right)$  where the probability current density can be defined as  $j_s(\psi)$ . [5]

<sup>2</sup>Here by gauge invariant phase we mean, e.g. that the expression  $\vec{\nabla} \varphi(t, \mathbf{x})$  will remain unchanged under using gauge transformations, that is, if we transform  $\varphi_0(t, \mathbf{x}) \rightarrow \varphi_0(t, \mathbf{x}) + \frac{q_s}{\hbar} \chi(\mathbf{x})$  and  $\vec{A}(t, \mathbf{x}) \rightarrow \vec{A}(t, \mathbf{x}) + \vec{\nabla} \chi(\mathbf{x})$ , where  $\chi(\mathbf{x})$  is any scalar field, we would see that the phase and subsequently supercurrent density will be invariant under these transformations. For those reader who are interested to know more that how this gauge invariant and combination come to the play, we refer to the Ginzburg–Landau theory.

In a typical JJ experiment, we usually apply a current that flows through a JJ and then we measure the output DC voltage. A commonly used electrical circuit model to measure the voltage across the JJ is called a Resistively Capacitively Shunted Junction (RCSJ) model. This circuit is schematically depicted in fig. 1.2,

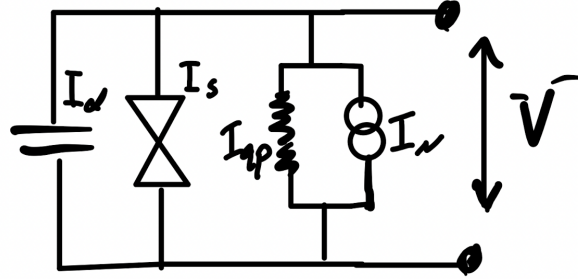


Figure 1.2: Schematic electronic equivalent circuit of JJ and a RCSJ.

According to Kirchhoff's law one can write the constant total current  $I = I_d + I_{qp} + I_s + I_N$ , which is coming from the current source divides into four components,

- (I) the supercurrent  $I_s = I_0 \sin [\varphi(t)]$ ;
- (II) dissipative (quasiparticle) current  $I_{qp} = \frac{V}{R_N}$  ; where  $R_N$  is a shunt resistor;
- (III) displacement current  $I_D = C_J \dot{V}$  ; where  $C_J$  is a capacitance across junction;
- (VI) Current noise source  $I_N(t)$ . Thus

$$I = I_0 \sin [\varphi(t)] + \frac{V(t)}{R_n} + C_J \frac{dV(t)}{dt}, \quad (1.6)$$

which can be rewritten using eq. (1.4) via Josephson phase,  $\varphi$  instead of  $V$  as

$$I = I_0 \sin (\varphi) + \frac{1}{R_n} \frac{\Phi_0}{2\pi} \dot{\varphi} + C_J \frac{\Phi_0}{2\pi} \ddot{\varphi}. \quad (1.7)$$

One can also derive the eq. (1.7) as the equation of motion (EoM) of a particle with coordinate  $\varphi$  moving in a potential energy  $U(\varphi)$ , using the Euler–Lagrange equation.

The Josephson potential energy  $U(\varphi)$  can be written as a cosinusoidal function

$$U(\varphi) \equiv E_J(1 - \cos \varphi - \gamma\varphi), \quad (1.8)$$

where  $\gamma \equiv I/I_0$  is the normalized bias current and  $E_J \equiv I_0\Phi_0/2\pi$  is the so-called Josephson coupling energy. In the fig. 1.3, the Josephson potential is plotted for different values of the  $\gamma$ . We observe that when  $\gamma = 0$ , we have a mirror-symmetric potential (purple curve), and as  $\gamma$  increases, the potential becomes tilted. The shape of  $U(\varphi)$  resembles an old-fashioned washboard, thus it is referred to as a tilted washboard potential. It is evident that the tilt of the potential arises from  $\gamma$ . Specifically, the frequency of particle motion on the purple, green, and red curves with  $0 \leq \gamma < 1$  exhibits periodic oscillation, whereas on the blue curve with  $\gamma \geq 1$ , the particle does not exhibit periodic oscillation. [7]

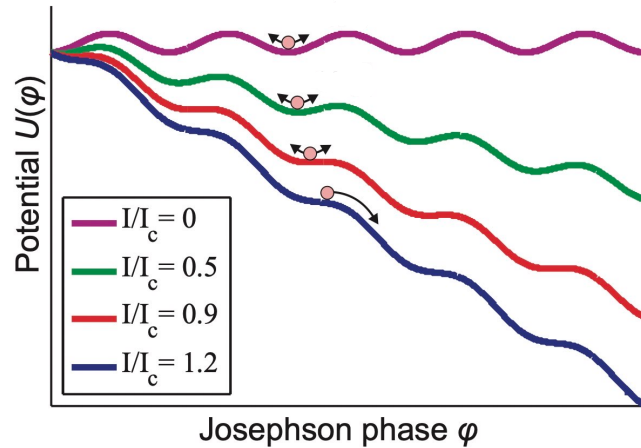


Figure 1.3: Plots of tilted washboard potential  $U(\varphi)$  for several values of the tilt (bias current)  $\gamma$ . Phase-particle, trapped in the minimum at  $\gamma < 1$  escapes from the minimum when  $\gamma \geq 1$  and slides down the potential.

It is often practical to use normalized units, therefore we introduce a new normalized time parameter  $\tau \equiv \frac{t}{\tau_c} = \frac{t}{2\pi e I_0 R} \Phi_0$ . So that eq. (1.7) becomes

$$-\gamma + \sin [\varphi(\tau)] + \frac{d\varphi}{d\tau} + \beta_c \frac{d^2\varphi}{d\tau^2} = 0, \quad (1.9)$$

where  $\beta_c \equiv \frac{\omega_c^2}{\omega_p^2} = \frac{2\pi}{\Phi_0} I_0 R_N^2 C$  is so called Stewart-McCumber parameter.

## 1.2 Current Voltage Characteristic ( $I$ - $V$ )

Now let us see how a dc current-voltage characteristic (IVC) of the JJ looks like. In an experiment, we usually apply different values of dc currents  $I$  and measure an average (dc) voltage across the junctions for each value of  $I$ ,  $\bar{V}(I)$ . Given the known periodic phase evolution  $\varphi(t)$ , the averaged voltage is calculated as follow

$$\bar{V}(I) = \frac{1}{T} \int_0^T V dt \stackrel{(1.4)}{=} \frac{1}{T} \int_0^T \frac{\Phi_0}{2\pi} \frac{d\varphi}{dt} dt = \frac{1}{T} \frac{\Phi_0}{2\pi} \overbrace{[\varphi(T) - \varphi(0)]}^{2\pi} = \frac{\Phi_0}{T}, \quad (1.10)$$

where we use 2nd Josephson equation in the second equality,  $T = \frac{2\pi}{\omega}$  is the period of the particle trapped in the symmetric Josephson potential. (e.g.  $\gamma = 0$ ). eq. (1.9) and (1.10) together can be used to obtain the typical IVC for different values of  $\beta_c$  as shown in fig. 1.4

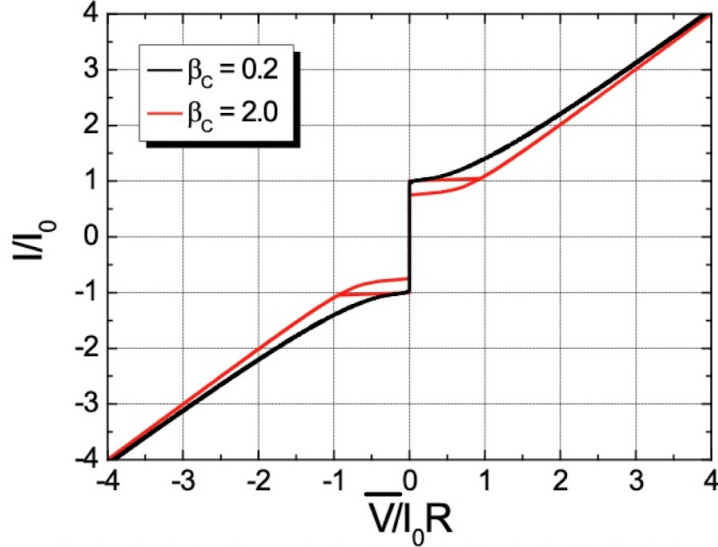


Figure 1.4: Current Voltage Characteristic, IVC of a symmetric potential.

For  $\beta_c \ll 1$  where friction term is dominant  $\dot{\varphi}$  one can ignore the last term ( $\beta_c \ddot{\varphi}$ ) in the eq. (1.9). It leads to a nonhysteretic IVC shown by black curve in fig. 1.4. In this case, it is calculated that one can find the period of particle  $T = \frac{2\pi\tau_c}{\sqrt{\gamma^2 - 1}}$ , and obtain averaged voltage

$$\bar{V} = \begin{cases} I_0 R \sqrt{\gamma^2 - 1} & \text{if } \gamma \leq 1, \\ -I_0 R \sqrt{\gamma^2 - 1} & \text{if } \gamma > 1, \\ 0 & \text{otherwise.} \end{cases} \quad (1.11)$$

For  $\beta_c \gg 1$ , the inertia term  $\ddot{\varphi}$  in eq. (1.9) becomes dominant and it leads to a hysteretic IVC (the red curve in the Fig. 1.4). In this case, e.g. one can investigate how the thermal fluctuation noise  $I_N(t)$  could characterize and adjust the hysteresis shown by the red curve in the fig. 1.4 by adding  $I_N(t)/I_0$  to the  $\gamma$  in the potential eq. (1.8).

To emphasize our point, we would like to highlight that the IVC is completely symmetric. In other words,  $\bar{V}(I) = -\bar{V}(-I)$ . [7]

### 1.3 Josephson Junction in a Magnetic Field

In the following, we will study the dependence of the IVC on the external magnetic field applied  $H$  to JJ. In particular, we are interested in the dependence of  $I(H)$ . First we determine how magnetic field affects the gauge invariant phase differences across our the JJ barrier, and then insert the phase differences across the JJ  $\varphi$  into the definition of the supercurrent density  $j_s(\varphi)$ . Finally we will integrate it over the JJ area to obtain the total supercurrent over the junction,  $I_s(H) = \int j_s(\varphi)dA$ . This  $I_s(H)$  may take a range of values. We are interested to find a min or max one correspondence to  $I_c$ . In [7] the author considers a JJ with a rectangular geometry for the sake of simplicity, and calculated the applied magnetic field induces a gradient of phase differences  $\varphi$  given by

$$\frac{d\varphi}{dx} = \frac{2\pi}{\Phi_0} Bd_{\text{eff}} \quad (1.12)$$

where  $d_{\text{eff}}$  is the effective magnetic thickness of the JJ. Without loss of generality, we assume a homogeneous applied magnetic field,  $B(t, x) \equiv B(x)$  which is applied along  $y$ -direction,  $B(x) \equiv B_y(x)\hat{y}$ , and perpendicular to the JJ surface,  $(x, z)$ . Additionally we notice here, by the Ampère–Maxwell equation we have  $\vec{\nabla} \times B_y = \frac{\partial B_y(x)}{\partial x}\hat{z} = \mu_0 j_z(x)$ . Now by taking derivative of eq. (1.12) with respect to  $x$  and using the Ampère–Maxwell equation we will get

$$\frac{\partial^2 \varphi(\mathbf{x})}{\partial x^2} = \frac{2\pi}{\Phi_0} d_{\text{eff}} \frac{\partial B_y(\mathbf{x})}{\partial x} = \frac{1}{\lambda_j^2} \frac{j_z(\mathbf{x})}{j_0} = \frac{1}{\lambda_j^2} \sin \varphi(\mathbf{x}) \quad (1.13)$$

where  $\lambda_j$  is so called the Josephson penetration,  $\lambda_j \equiv \left( \frac{\Phi_0}{2\pi\mu_0 d_{\text{eff}} j_0} \right)^{1/2}$ . We notice that for small applied magnetic field we can use Taylor expansion ( $\sin \varphi \approx \varphi$ ) and solve eq. (1.13) to obtain  $\varphi(x) = \varphi(0)e^{-x/\lambda_j}$ . Now if we assume that our junction has length  $L$  smaller than Josephson penetration length  $\lambda_j$ , then  $B_y$  fully penetrates

into the JJ and becomes constant i.e.  $B(x) \approx const$  by the second London equation  $B_y(x) = B_y(0)e^{-x/\lambda}$ . Thus we can easily take the integral of eq. (1.12) by pulling  $B$  out of the integral and obtain

$$\varphi(t, \mathbf{x}) = \varphi_0 + \frac{2\pi}{\Phi_0} B d_{\text{eff}} x. \quad (1.14)$$

Hence one can rewrite the eq. (1.5) as follow

$$I(x) = W \int j_c(x) \sin(\varphi(t, x)) dx = W \int j_c(x) \sin\left(\varphi_0 + \frac{2\pi}{\Phi_0} B d_{\text{eff}} x\right) dx \quad (1.15)$$

where  $W$  is the width of the JJ and  $j_c(\mathbf{x})$  is a critical current density which can be uniformly (e.g.  $j_c(\mathbf{x}) = const$ ) or non-uniformly (e.g.  $j_c(\mathbf{x}) = j_c(x, y)$ ) distributed and so can be realized by the choice of geometry and the presence of magnetic field. The supercurrent in general is investigated in [6] for different choices of current density and geometry. One can rewrite eq.(1.15) for a rectangular geometry of a BJJ (e.g. for a JJ with length  $|x| \leq L/2$  and width  $W$ ) as

$$I(\mathbf{x}) = W \int_{-L/2}^{L/2} j_c(x) \sin(\varphi) dx = W \operatorname{Im} \left\{ e^{i\varphi_0} \int_{-L/2}^{L/2} j_c(x) e^{i2\pi B d_{\text{eff}} x / \Phi_0} dx \right\} \quad (1.16)$$

The eq.(1.16) can be then maximized with respect to  $\varphi_0$ ,  $\left| \frac{dI}{d\varphi_0} = 0 \right|$  and give us

$$I(x) = W \left| \int_{-L/2}^{L/2} j_c(x) e^{i2\pi B d_{\text{eff}} x / \Phi_0} dx \right| \quad (1.17)$$

This is the maximum Josephson current at any given applied magnetic field,  $H$ . Now if we assume a uniform critical current distribution i.e.  $j_c(x) = const$  inside the

JJ, then the eq.(1.17) gives the famous Fraunhofer dependence

$$I_c(\Phi_J/\Phi_0) = I_0 \cdot \left| \frac{\sin\left(\pi \frac{\Phi_J}{\Phi_0}\right)}{\pi \frac{\Phi_J}{\Phi_0}} \right| = I_0 \cdot \left| \text{sinc}\left(\pi \frac{\Phi_J}{\Phi_0}\right) \right| \quad (1.18)$$

where  $\Phi_J = Bd_{\text{eff}}L$  is the total magnetic flux inside the junction and  $I_0 = j_c \times A_J = j_c \cdot W \cdot L$ . One can plot critical current versus flux  $I_c(\Phi_J)$  as shown in fig 1.5. For all values of  $\Phi_J$ , the eq. (1.18) can be rewritten as  $I_c(\Phi_J/\Phi_0) = \pm I_0 \cdot \left( \text{sinc}\left(\pi \frac{\Phi_J}{\Phi_0}\right) \right)$  which is plotted in the fig. 1.5. The signs also indicate maximum ( $I_{c+}$ ) and minimum ( $I_{c-}$ ) critical currents.

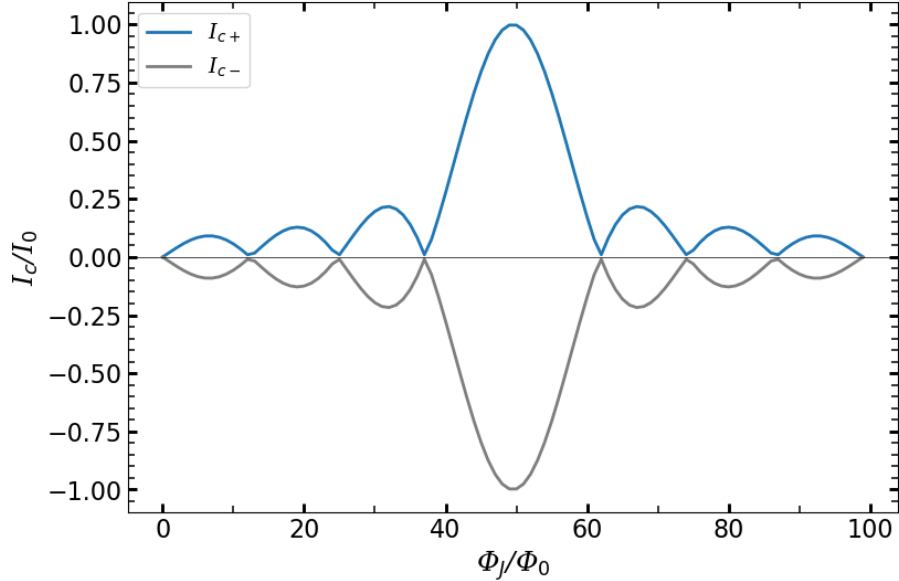


Figure 1.5: Negative and positive  $I_c(\Phi_J)$  are symmetric for fixed  $\Phi_J$ . For example, here for the fixed value of  $\Phi_J/\Phi_0 = 44.5$  we observe,  $|I_{c+}/I_0| = |I_{c-}/I_0| = 0.75$ .

To this end, we would like to point out that the  $I_c(\Phi_J)$  representation is symmetric with respect to the current polarity, i.e, for any fixed value of the flux  $\Phi_J$  we find that  $|I_{c+}| = |I_{c-}|$ . [6]

# Chapter 2

## Theory of Ratchet

### 2.1 An Overview of Josephson Ratchet

When discussing a ratchet, the simplest model we have in mind is a periodic asymmetric potential<sup>1</sup> where a particle moves under the action of stochastic force with zero time averaged, fig. 2.1 (a). Such a force pushes the particle back and forth, but on average the force does not push the particle anywhere forward or backward. (i.e., the particle could not pass the potential well). However, because of the asymmetry of the potential, in some cases one can observe a net transport in a particular direction. Consequently, the random force with zero time average can be transformed into directed particle motion, enabling the particle to perform useful work. We will delve further into this concept in the subsequent sections of this chapter

Before proceeding, we would like to clarify that in the following discussion, when we refer to the averaged velocity  $\langle \dot{\varphi} \rangle$  of the particle, it is equivalent to the averaged voltage as described by eq. (1.4). Similarly, when we mention the application of current, as indicated in eq. (1.7), it is analogous to applying a force.<sup>2</sup>. Hence, when

---

<sup>1</sup>by asymmetrical we mean reflexion asymmetry,  $U(-\varphi) \neq U(\varphi)$

<sup>2</sup>The Newtonian force for a stationary potential can be written as  $F = -\nabla_\varphi U(\varphi)$ . Now if we use the Josephson potential eq. (1.8) we would get  $F \propto \gamma$  which means that applied current is proportional to force.

we mention the application of a dc current to the system, it is synonymous with applying forces.

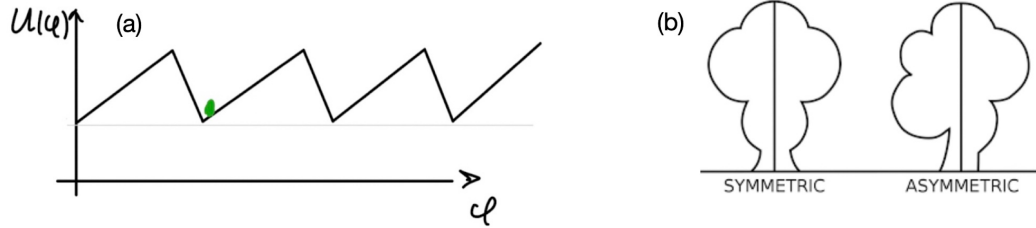


Figure 2.1: (a) An example of a particle trapped in a schematic asymmetric potential (b) indicates schematically meaning of asymmetric.

So far we studied the symmetric Josephson potential in detail (see eq. (1.8) and fig. 1.3). However to construct a Josephson ratchet we need to design an asymmetric Josephson potential. We schematically show this kind of potential in fig. 2.1(a).

Similar to Chapter. 1, in order to determine the IVC, one can derive averaged voltage depend on the current from an EoM analogous to eq. (1.9) but this time for an asymmetric Josephson potential instead of symmetric potential. A non-hysteretic IVC for asymmetric potential is schematically depicted in the fig. 2.2,

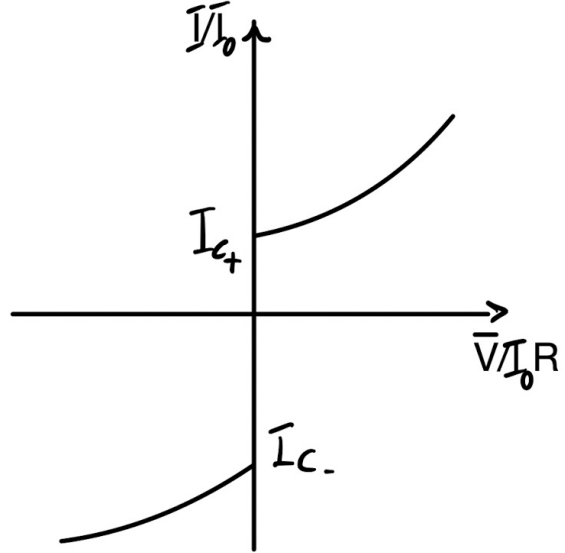


Figure 2.2: Schematic example of a non-hysteretic IVC for an asymmetric Josephson potential.  $I_{c+}$  is positive critical current and  $I_{c-}$  is negative critical current.

We clearly observe that  $|I_{c-}| \neq |I_{c+}|$ , resulting in an asymmetric IVC, which is in contrast to what we obtained for the symmetric Josephson potential. This inequality in  $I_c$  values is attributed to the fact that in asymmetric potential the maximum slopes of the potential in the left/right directions are different. Therefore the force (applied current) needed to overcome this slope (critical current) is also different for polarities. We can now quantify the degree of asymmetric by the asymmetry parameter  $\mathcal{A}$ , which is the ratio of maximum slopes of the potential in the left/right directions

$$\mathcal{A} \equiv \frac{|I_{c-}|}{|I_{c+}|}. \quad (2.1)$$

Later, we will see that  $\mathcal{A}$  is one of the key parameters defining the performance of the ratchet.

### 2.1.1 Josephson Ratchet Operation

If the IVC exhibits a similar characteristic as shown in fig. 2.2, it is possible to operate a ratchet in the deterministic regime and construct a rectifier. Typically, a rectifier is achieved by applying an ac signal and obtaining a dc output signal. In our specific case, we apply an ac current and observe the ratchet effect through the response of the dc output. This effect can be accurately interpreted using a rectification curve  $\langle V_{dc}(I_{ac}) \rangle$ . Fig. 2.3 schematically illustrates the rectification curve,

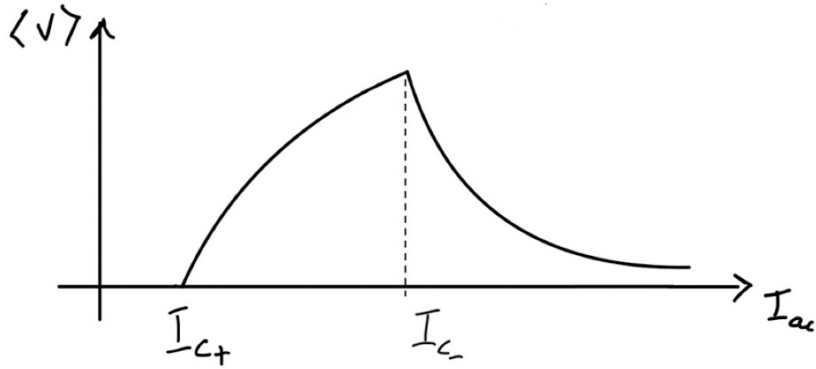


Figure 2.3: A rectification curve represents an averaged velocity of a particle ( $\langle \dot{\varphi} \rangle \propto V$ ) as a function of an applied ac-drive amplitude  $I_{ac}$ . The interval between  $I_{c+}$  and  $I_{c-}$  is called operation interval or the rectification window. Its size is defined as  $\Delta \equiv I_{c-} - I_{c+}$ .

When an alternating current  $I_{ac}(t) = I_{ac} \sin(\omega t)$  is applied, it can be understood as tilting the potential back and forth at a frequency of  $\omega$ . However, for small tilting amplitudes  $I_{ac}$ , we find that the particle remains trapped within the potential well, resulting in an average velocity (voltage) of zero. As we gradually increase  $I_{ac}$  up to  $|I_{c+}|$ , the averaged voltage  $\langle V_{dc}(I_{ac}) \rangle$  remains zero. However, beyond this point, the particle starts moving forward until it reaches its maximum average velocity at  $|I_{c-}|$ . Subsequently, it ceases to move and gradually approaches zero velocity. The range between  $I_{c+}$  and  $I_{c-}$  is known as the rectification window (RW), representing

the interval during which the particle, confined within the asymmetric potential, can move during a fraction of the positive and negative semi-periods of the ac drive.

We observe that a larger asymmetry parameter results in a wider RW. In the absence of asymmetry (i.e., in the case of a symmetric Josephson potential with  $\mathcal{A} = 1$  or  $|I_{c+}| = |I_{c-}|$ ), the rectification curve (average velocity) remains zero, and the particle does not move forward. This occurs because the net average force exerted on the particle from both left and right sides of the symmetric potential well is zero. This can be seen, for example, in the purple curve depicted in fig. 1.3.

A relevant question arises: How effectively good is a ratchet? How can we characterize its performance? Obviously, we want a ratchet to work not only for a certain amplitudes of the input signal, but for a very wide range of amplitudes, ideally, from a small amplitude to a very large amplitude. However as we saw in the fig. 2.3 the ratchet does not move for the small and very large amplitudes, and there is only a limited range of amplitudes (the RW) in which the rectification occurs ( $\langle V \rangle \neq 0$ ). Therefore To achieve a broad operational range for the ratchet, we aim to maximize the size of the RW. This entails minimizing  $|I_{c+}|$  and maximizing  $|I_{c-}|$ . Consequently, a larger asymmetry parameter  $\mathcal{A}$  leads to an expanded interval of operation, enabling a wider range of amplitudes in which the ratchet can function effectively.

However, even if the ratchet is capable of rectification, it does not yet generate useful work or deliver rectified power to a load. In such a scenario, we refer to the ratchet as being idle. To prevent the ratchet from being idle, it needs to be loaded with a counterforce, typically in the form of a dc current. This counterforce tilts the potential and pushes the particle in the opposite direction to the ratchet motion. If the ratchet effect is stronger than this counterforce, the particle will overcome the constant (counter) slope and ascend, thereby performing useful work. In fig. 2.4, a loaded ratchet is schematically depicted.

Regarding the potential additive (represented by  $\gamma$  in eq. (1.8)), the dc current  $I_{dc}$  tilts the potential, enabling the particle to climb and produce the desired useful work.

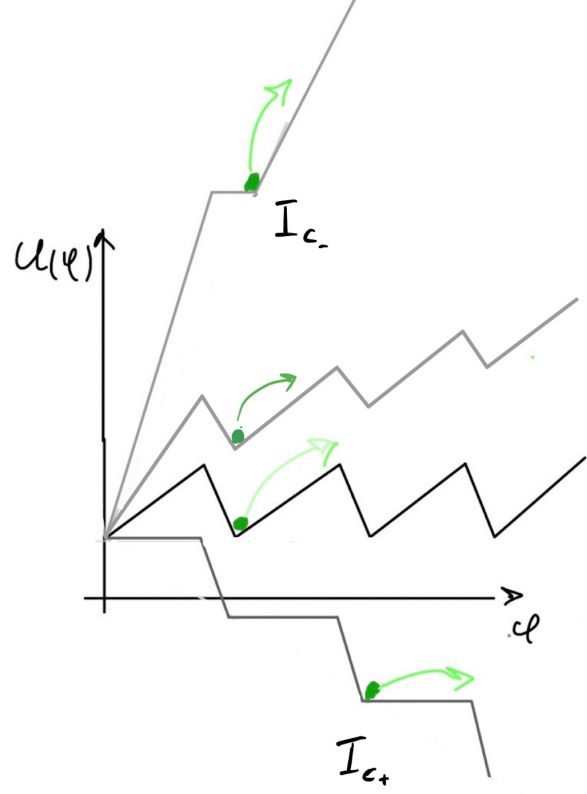


Figure 2.4: A ratchet potential for  $I_{dc} = 0, I_{c-}, I_{c+}$ .

Hence, in an experimental setup, it is possible to load a ratchet by applying different values of a dc bias current, denoted as  $I_{dc}$ , in the opposite direction to the net motion. This counterforce, which causes the ratchet to come to a halt, is referred to as the stopping current. As illustrated in fig. 2.4, if the ratchet transport initially occurs in the positive direction along the  $\varphi$ -axis, we apply  $I_{dc} < 0$ . This results in a potential tilt of  $-I_{dc} \cdot \varphi$ , allowing the particle to perform work through the ratchet effect.

The rectification curve for a loaded ratchet is schematically depicted in Figure 2.5.

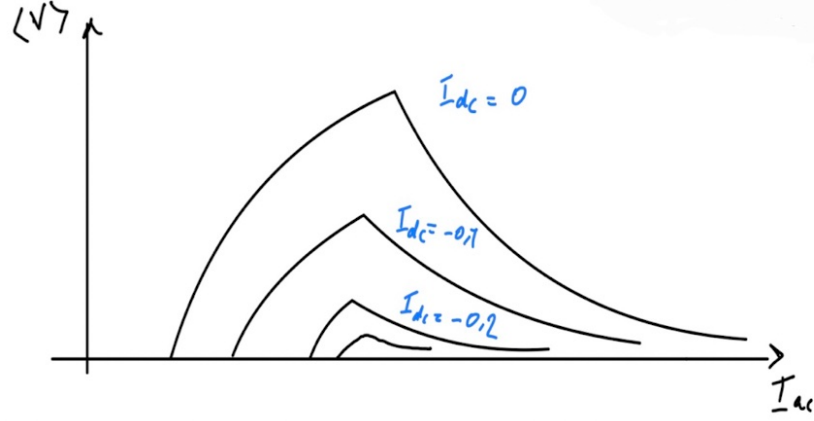


Figure 2.5: The schematic loaded ratchet up to countercurrent  $|I_{dc}| = 0.2 \mu\text{A}$ .

As depicted in Figure 2.5, it is evident that gradually increasing the load  $I_{dc}$  leads to a reduction in the size of the rectification curve and the values of  $\bar{V}_{dc}$ . This reduction is generally the trade-off required to load the ratchet and compel the particle to perform useful work. Specifically, we observe that as the load  $I_{dc}$  increases, the operational range in terms of  $I_{ac}$  decreases. However, in this narrower interval, the particle is compelled to move against the ratchet motion and produce useful power. Our primary objective is to maximize both the rectification windows (RWs) and the value of the stopping current.

To summarize this section, let us consider an example simulation of a ratchet<sup>3</sup> that was studied in [2] and [3]. The simulations were conducted in a quasistatic regime, allowing for the acquisition of information about the ratchet's operation solely from its asymmetric IVC. The authors generated a step-like asymmetric IVC, as shown in fig. 2.6(a), and simulated various figures of merit based on this IVC. fig. 2.6(b) presents the simulation results for a loaded rectification curve.

---

<sup>3</sup>A deterministic underdamped Josephson vortex ratchet consisting of a long Josephson junction with  $L \geq \lambda_j$ .

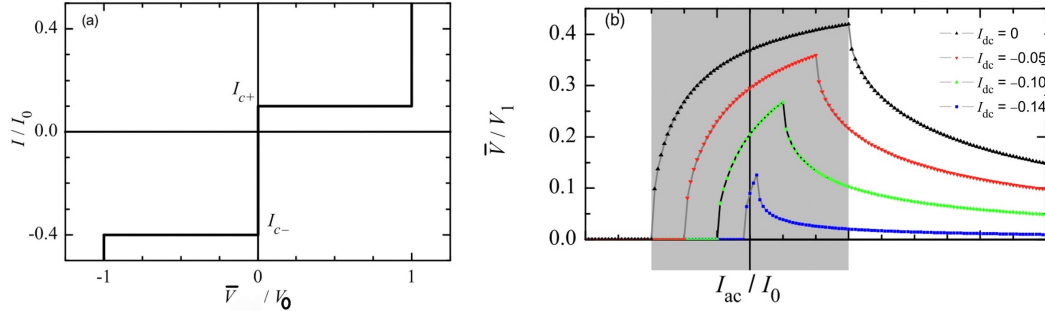


Figure 2.6: (a) Asymmetric IVC with  $\mathcal{A} = 4$ . (b) The rectification curves for several values of  $I_{dc}$ .

The black curves in fig. 2.6(b) correspond to the case where  $\mathcal{A} = 4$  and  $I_{dc} = 0$ . By loading the ratchet and increasing  $I_{dc}$  (colored curves), we observe that the rectification window (RW) becomes shorter. Consequently, the asymmetry parameter is reduced<sup>4</sup>. However, within this shorter interval, the particle can perform more useful work and achieve higher efficiency, as we will explain in the following subsection.

### 2.1.2 Efficiency

Efficiency is defined as useful output dc power  $\bar{P}_{\text{out}}$  divided by the total input power consumed by the system  $\bar{P}_{\text{in}}$

$$\eta \equiv \frac{-\bar{P}_{\text{out}}}{\bar{P}_{\text{in}}} \quad (2.2)$$

As a case study, the efficiency of the model investigated in [2] is presented in fig. 2.7(e). The black curve represents the idle ratchet, while the colored curves correspond to loaded ratchets with different values of  $|I_{dc}|$ . From fig. 2.8(c), we observe that as  $I_{ac}$  increases, the input power  $\bar{P}_{\text{in}}$  also increases, reaching its maximum at the end of the rectification window (RW). The ratchet operates with maximum efficiency  $\eta$  at the beginning of the RW for any stopping force, as shown in fig. 2.7(e). Fur-

---

<sup>4</sup>To see this, one can express the asymmetry parameter in terms of the rectification window as  $\mathcal{A} = \frac{I_{c+} + \Delta}{I_{c+}}$ , making it clear that decreasing  $\Delta$  leads to a reduction in asymmetry.

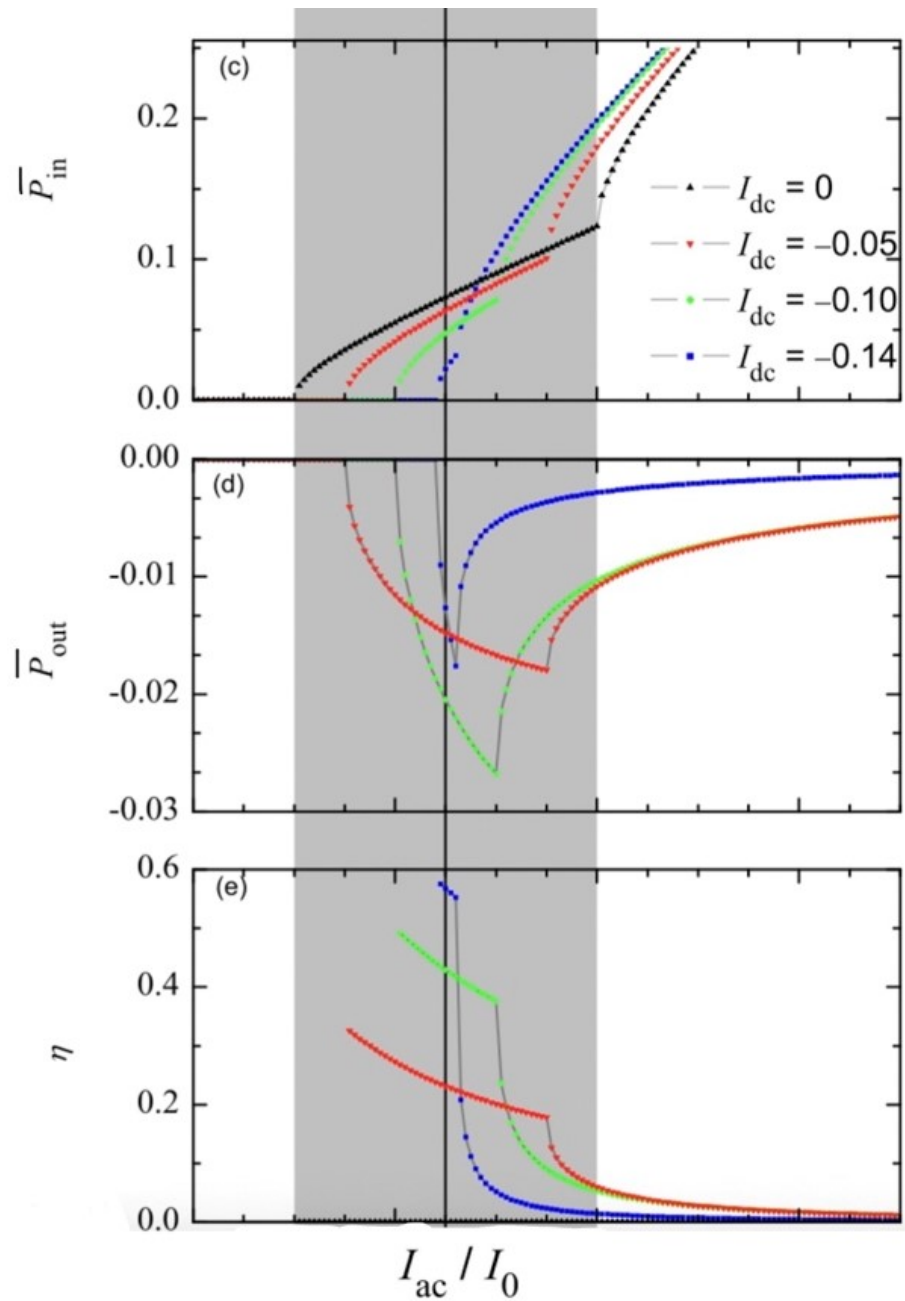


Figure 2.7: (c) Average input ac power  $\overline{P}_{\text{in}}$ , (d) average output dc power  $\overline{P}_{\text{out}}$ , (e) efficiency  $\eta$ .

thermore, we notice that increasing  $|I_{dc}|$  results in a shorter operation interval but a higher efficiency. In [3], it was demonstrated that the maximum efficiency achievable in principle is determined solely by the asymmetry of the potential, given by  $\eta_{\max} = \frac{I_{c-} - I_{c+}}{I_{c-} + I_{c+}}$ . Overall, we can observe that a higher asymmetry leads to a higher maximum efficiency.

### 2.1.3 Theoretical Design of JJ with In-line Geometry

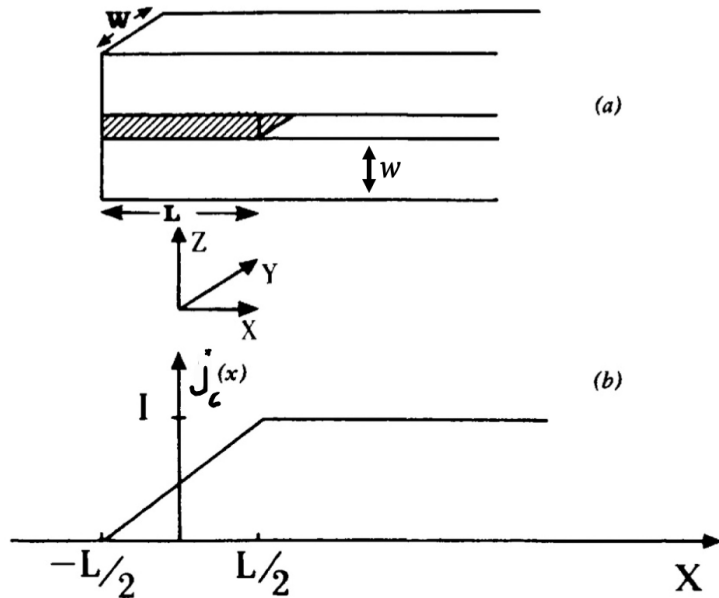


Figure 2.8: (a) The in-line geometry of a (JJ) consists of superconducting where the dashed line representing the barrier JJ surrounded with superconductors. (b) The critical density  $j_c$  as a function of distance  $x$ .

In the classical textbook on the Josephson effect [6], Barone *et al.* considered an in-line JJ geometry, fig. 2.8(a). In this geometry the bias current fed from the right side flows through the Josephson junction (the dashed hatched region) produces the called self-field.<sup>5</sup> The self-field together with the applied external magnetic field  $H_e$

---

<sup>5</sup>To be more precise, by solving continuity equation  $\left(\nabla_x \left(\frac{j_c}{W}\right) = J_c\right)$  with the boundary condition  $j_c(-L/2) = 0$  and  $j_c(L/2) = 1$  we will obtain the total uniform current density  $\left(j_c(x) = W J_c \left(x + \frac{L}{2}\right)\right)$  inside of a BJJ as shown in the fig. 2.8(b). Then, one can write down

tilts  $I_c$  as shown in fig. 2.9. In the chapter 5.1 of [6], it is explained how the change of the geometry changes the magnetic flux, current density and subsequently the dependence of maximum supercurrent on flux. By integrating the Josephson current density  $J_c$  over the line  $x$  (see fig. 2.8) and maximizing it with respect to  $\Phi_0$  across the junction, one would obtain the maximum Josephson current through Josephson junctions as

$$\frac{I_c(f)}{I_0} = \left| \frac{\sin \pi \left( f + f^M \frac{I_c(f)}{I_0} \right)}{\pi \left( f + f^M \frac{I_c(f)}{I_0} \right)} \right| \quad (2.3)$$

where for the simplicity we have defined normalized flux  $f \equiv \Phi_J/\Phi_0$  and the geometric normalized flux  $f^M \equiv \Phi_s^M/\Phi_0$ .  $\Phi_J = dLH_e$  is the total applied flux inside JJ.  $\Phi_s^M$  describes the strength of the in-line geometry and is given by

$$\Phi_s^M = \frac{\mu_0 L d I_0}{2w}. \quad (2.4)$$

One would rewrite the above equation in terms of  $f^M$  and  $\lambda_j$  as  $L = \lambda_j \sqrt{4\pi f^M}$ .  $\Phi_s^M$  describes how much the  $I_c(H)$  plot is skewed and deviates from the symmetric dependence as shown in the fig. 2.9. We notice that at  $f^M = 0$  the maximum supercurrent  $I_c(f)$  becomes unskewed and symmetric as the Franhufer pattern  $(I(f) = I(-f))$  given by the eq. (1.18) and shown in the fig. 1.5. In the above formula  $W$  is the width (in the direction perpendicular to the plane of the picture in the fig. 2.8(a)) and  $L$  is the length of JJ along  $x$  direction.  $I_0 = WLj_c$  is the maximum value of supercurrent  $I$ , where  $j_c$  is the uniform Josephson current density,  $d$  is the effective magnetic thickness, whose value is given by  $d = t + 2\lambda_{\text{eff}} \coth(w/\lambda_{\text{eff}})$ , where  $\lambda_{\text{eff}} = \lambda \coth(t/\lambda)$  is the effective London penetration depth,  $t$  is the thickness of insulator,  $w$  is the distance between barrier JJ and the superconductor as shown in the fig. 2.8(a)), and  $\lambda$  is the London penetration depth.

---

the total magnetic field originated from the current density and then derive maximum current as eq. (2.3) for small junction compare to Josephson penetration depth.

The eq. (2.3) defines an implicit function of  $I(f)$  on the flux. It can not be rewritten in an explicit form. Therefore, we find the solution  $I(f)$  numerically. We wrote a Python script to solve eq. (2.3) numerically which uses the bisection method to find the solution. The plot of  $I(f)$  is calculated for several fixed values of  $f^M$  are shown in the fig. 2.9. One can see the skeweness of  $I(f)$  depends on  $f^M$ . Visually, if we draw, say, a vertical line fixed value of  $f$ , we clearly notice that  $|I_{c+}| \neq |I_{c-}|$  for most of the  $f$  values. Thus one can calculate the asymmetry parameter  $\mathcal{A}$ .

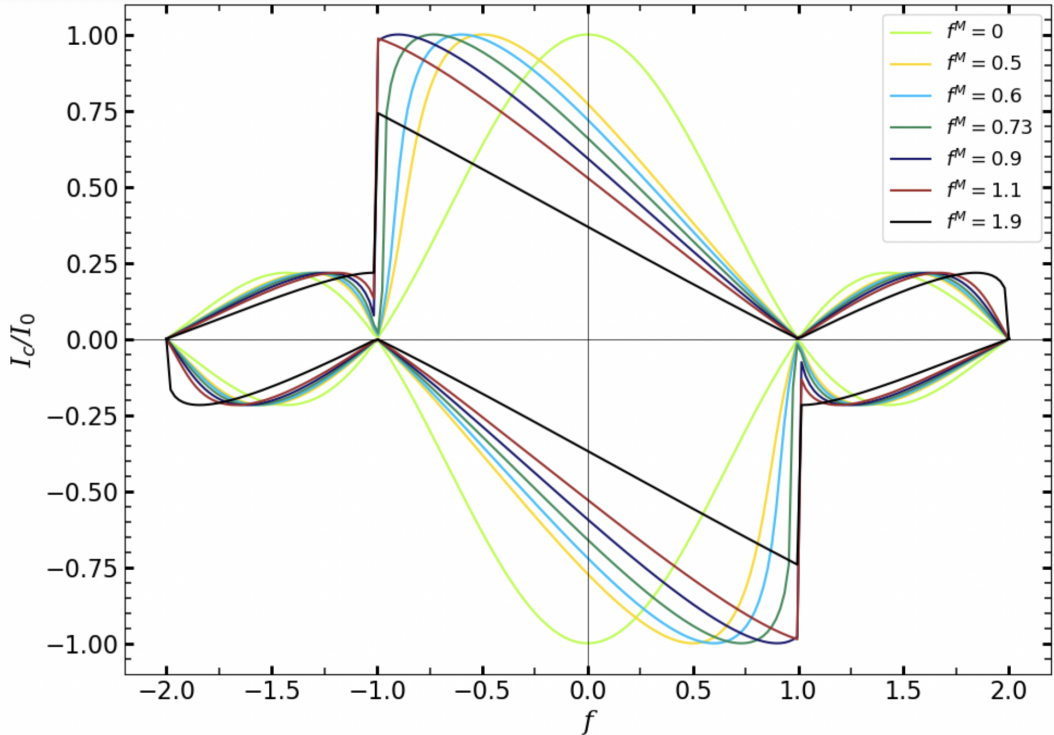


Figure 2.9: Asymmetric  $I_c(f)$ , which is obtained by simulation of solution of eq. (2.3).

Note also the maximum asymmetry at the optimum point  $f_{\text{opt}}$  (where the asymmetry is maximum) of  $f$  is symmetric under changing the sign of  $f$ . Now let us find the behavior of  $\mathcal{A}$  as a function of  $f$  and  $f^M$ . In the fig. 2.10(a) we see how the asymmetry parameter  $\mathcal{A}$  depends on  $f$  for different fixed values of  $f^M$ . For example, for the blue curve ( $f^M = 0.6$ ) we find asymmetry parameter  $\mathcal{A} \approx 8$  for certain optimum value of  $f_{\text{opt}}$ . This maximum asymmetry value is just increasing by increasing the

value of  $f^M$ . In fig. 2.10(b) we show the dependencies of the maximum  $\mathcal{A}(f_{\text{opt}})$  to the  $f^M \in (0, 1.9]$  at the optimum value of  $f$ , and it is shown that how  $\mathcal{A}$  is growing by increasing  $f^M$ .

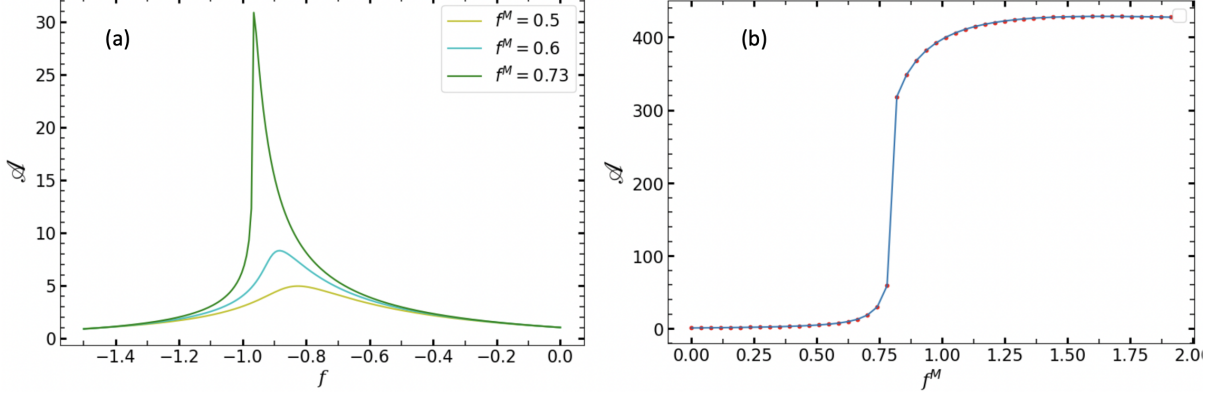


Figure 2.10: (a) Asymmetry parameter  $\mathcal{A}$  vs. magnetic flux  $f$  for different values of  $f^M$ ; (b) asymmetry parameter  $\mathcal{A}$  vs. strength of in-line geometry  $f^M$ .

Thus using the in-line JJs and proper applied normalized flux  $f$ , one is able to design a ratchet with asymmetry parameter i.e., up to the value  $\mathcal{A} \approx 400$  for the largest  $f^M \approx 1.9$ . We would emphasize here that the maximum asymmetry at the optimum magnetic point  $f_{\text{opt}}$  for the curve with high value of  $f^M$  is relatively high, see the fig. 2.10(b), because from some magnetic point (around  $f^M \approx 0.9$ ) onward we observe that increasing the value of  $f^M$  does not alter the optimum point. Instead, one of the critical currents, specifically  $I_{c+}$  in our case, tends to approach zero at a faster rate compared to the other one ( $I_{c-}$ ), which continues to increase. Consequently, this leads to an increase in the asymmetry parameter, approaching infinity as defined. However, it becomes evident in later experiments that achieving such high asymmetry is not feasible. In reality, the system is subject to substantial amounts of surrounding noise that significantly impact its behavior. These noises can introduce deviations in the optimal magnetic point, causing a substantial reduction in the actual asymmetry parameter compared to the intended target parameter. As

a consequence of this offset, one of the critical currents may not approach zero as predicted by the theoretical model we are observing.

We will examine the optimal target parameters for designing an effective ratchet in the next chapter, once we are prepared to commence the ratchet implementation.

# Chapter 3

## Fabrication and Implementation

### 3.1 Sample Information

The sample was prepared using commercial YBCO thin film produced by a company named Ceraco. The sample consist of a 2 inch LSAT substrate with 30 nm of  $\text{YBa}_2\text{Cu}_3\text{O}_7$  (YBCO) film and 20 nm of Au deposited on top. The detail information of the chip is provided by the company as shown in the fig. 3.1.

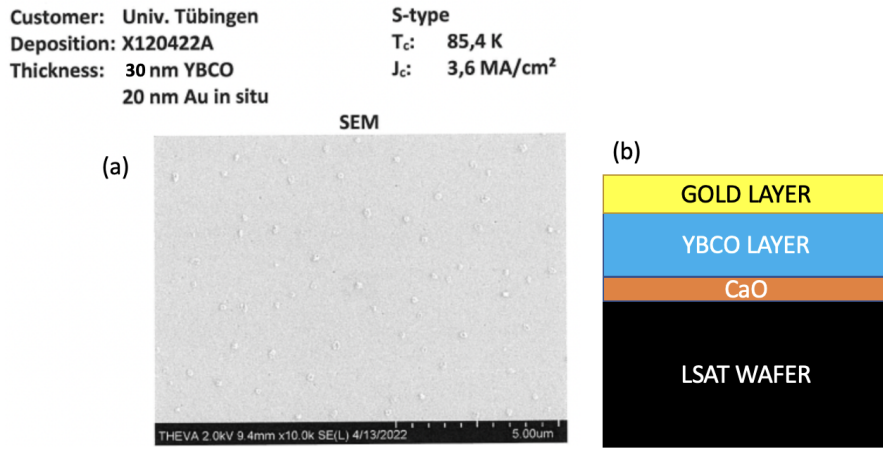


Figure 3.1: YBCO film on 2 inch LSAT wafer. (a) The picture of scanning electron microscope of the surface of the sample. The critical temperature  $T_c$ , the value of the current density  $j_c$ , and the other info are provided by Ceraco. (b) A schematic picture of the chip with its different layer deposition

## 3.2 Sample Layout

$1 \times 1 \text{ cm}^2$  chip is divided into four similar smaller chips of  $5 \times 5 \text{ mm}^2$ . Every small chip is labeled with letter A, B, C and D. The layout of each small chip is shown in the fig. 3.2. It consists of two columns of 18 bridges making 36 bridges in total. Each bridge has two contact pads on one side and all the bridges are connected to the main central line (vertical in the fig. 3.2) that is also connected to two ground pads from both sides.

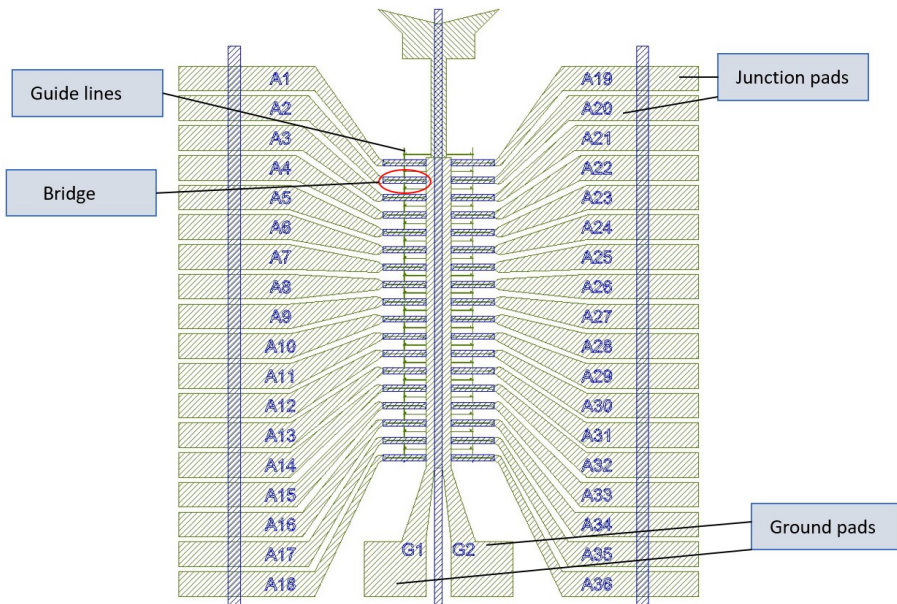


Figure 3.2: Layout of the small chip. The hatched light green areas correspond to the Au covered pads and the blue is the LSAT substrate, the guide lines are also covered by Au, and on the bridges Au is removed down to YBCO.

## 3.3 Sample Fabrication

The first step of the fabrication process starts with the dicing of 2 inches film into four pieces of  $5 \times 5 \text{ mm}^2$ . They are then cleaned in an ultrasound bath filled with acetone and then twice with isopropanol, also in an ultrasound bath. After dicing and cleaning, the sample is spin-coated with a photo-resist “ma-P1205” and later dried

on a hotplate at 90° Celsius for 210 seconds. Then, the chip is loaded into a maskless aligner model where the chip is patterned in two steps:

**(i). Etching of the gold:** Once the chip is inside the maskless aligner, a laser beam scans the layout patterned in the see fig. 3.3(a) which changes the properties of the photo-resist. The chip is taken out of the machine and the altered photo-resist is developed with “ma-D 331/S” for 50 seconds and quickly transferred to water to wash the extra developer away and again to another flask with water to clean again. Then the sample is dried and then the gold is etched by Argon ion beam. After the etching is finished, the remaining photo-resist is removed and spin-coated again in the same conditions as mentioned.

**(ii). Etching of the YBCO:** The chip is now again loaded into the maskless aligner to do the second ethching step, the same process as in step (i) is carried out but now the machine scans another mask see fig. 3.3(b). The photo-resist is modified again and so, after taking the chip out of the maskless aligner, is selectively developed with “ma-D 331/S” and rinsed in water twice. Then is dried again and the YBCO is etched with H<sub>3</sub>PO<sub>4</sub> 0,1photo-resist is removed once again and the chip is ready to be diced once more. The zoom in pictures of bridges after each steps of etching is shown in the fig. 3.4. [8]

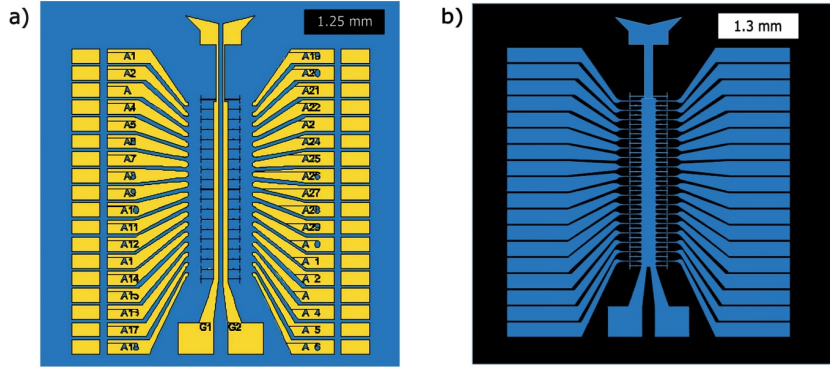


Figure 3.3: Mask used during the patterned process. (a) Mask used during step (i) for the etching of gold. The blue zone is where the gold has been removed and only YBCO remains. The yellow zones belong to where the gold still remains. (b) The mask used during step (ii) for the etching of YBCO. The areas in blue represent the regions where the YBCO still remains. The black area represents LSAT (substrate). Note that in the regions where the gold remains from the first step (for example, over the pads), has not been removed during the second step.

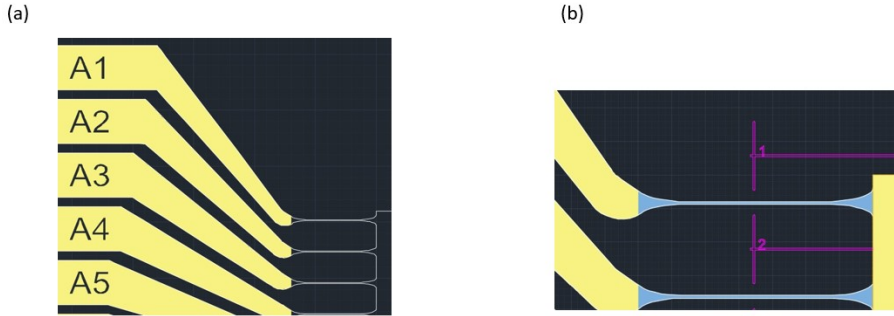


Figure 3.4: The microscope pictures of the sample after each step of the lithography process. (a) Picture of the pads after the first step. The dark areas are YBCO and the yellow areas are gold. (b) The picture of the bridges after the second step. The yellow area is gold, the dark area is LSAT, the blue area is YBCO where the junction will be finally irradiated and the purple lines are guide lines for our next step HIM

We are now ready to bring the sample to the Helium ion beam (He-FIB) to produce BJJ s and ratchets with focused (He-FIB).

### 3.4 He-FIB

We utilize a He-FIB (Helium-Focused Ion Beam) system with an energy of 30 keV to fabricate the Josephson barrier and create the BJJ (Biased Josephson Junction).

The process is illustrated in fig. 3.5, which provides a concise overview of the He-FIB technique.

## ORION NANOFAB - HELIUM ION MICROSCOPE

### Working Principle

The helium ions are produced at a tip of only three individual atoms, the trimer. Each of these atoms generates an ion beam in the helium atmosphere at the tip. The most intensive beam is selected and directed into the microscope's optics to reduce the beam diameter and to scan the focused beam sequentially in discrete locations in a raster x-y pattern on the specimen. At each discrete point, the interaction of the ion beam with the specimen produces secondary electrons. These secondary electrons are used for imaging as standard, whereby only SE from the top few nanometers of a surface contribute significantly to the signal.

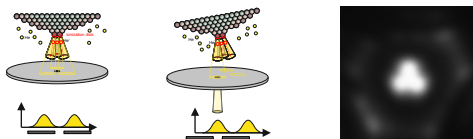
### Helium / Neon Ion Microscope

#### Technical Specifications

Scanning Ion microscope  
Gas Field Ion Source (GFIS) with helium and neon  
Field of view: 800 μm - 100 nm @ 8 mm working distance  
Resolution: 0.35 nm @ He 30 kV, 1.9 nm @ Ne 25 kV  
Beam energy: He 10 - 30 kV; Ne 10 - 25 kV  
Beam current: He 0.1 - 100 pA; Ne 0.1 - 50 pA  
Everhart Thornley Secondary Electron Detector  
Electron flood gun for charge compensation  
Advanced Nanopatterning  
Gas injection system with Pt-, W- or SiO<sub>2</sub>-precursor  
2 Kleindiek micromanipulators  
Plasma cleaner

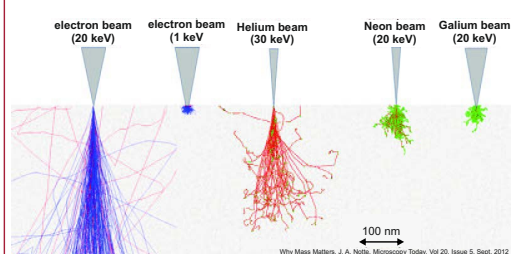


### Gas Field Ion Source (GFIS)



Typical performance metrics for a GFIS Gun  
Operating extraction voltage: 25 - 35 kV  
Operating Temperature: 60 - 90 Kelvins  
Base Pressure:  $< 4 \times 10^{-10}$  Torr  
Operating gas pressure:  $1 \times 10^{-7} - 5 \times 10^{-6}$  Torr  
Brightness:  $5 \times 10^9 \text{ A m}^{-2} \text{ sr}^{-1}$   
deBroglie wavelength @30 kV: ~ 0.080 pm  
Virtual source size: < 0.25 nm  
Total emitted current: ~ 150 pA

### Substrate Interaction



Simulations for 20 keV and 1 keV electron beams, a 30 keV helium beam, and 20 keV neon and gallium beams. The electron trajectories are shown in blue, and backscattered electrons are shown in red. The ion trajectories are shown in red, and the trajectories of recoiled sample atoms are shown in green. The simulated sample here is aluminum.

### GFIS GUN / Ion Optical Column

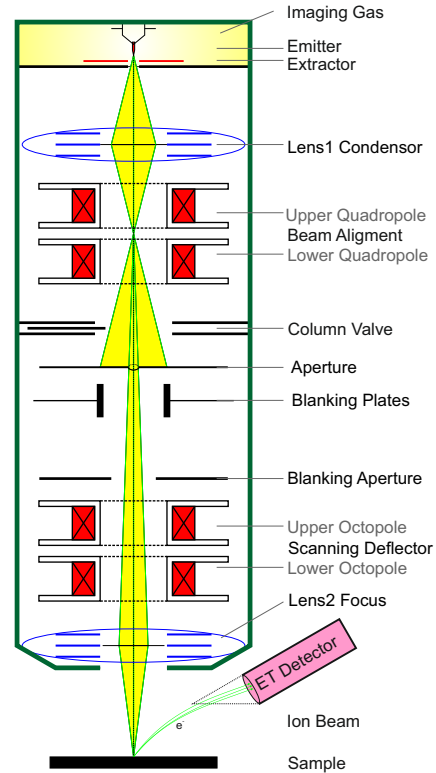


Figure 3.5: The poster of He-FIB.

The schematic illustration of irradiation ion is shown in the fig. 3.6.

We create the Josephson barrier depending on the Dose D by irradiating the bridge a long the line with a certain Dose (ion/nm). The Helium ion makes either a very thin (few nm) amorphous region or a line (also few nm width) with suppress  $I_c$  (changed doping) which play the role of Josephson barrier between two superconductors (BJJs). In the [9] it was experimentally shown that the critical current density  $j_c$  of the resulting BJJ depends on the irradiation dose,  $D$ , approximately as,

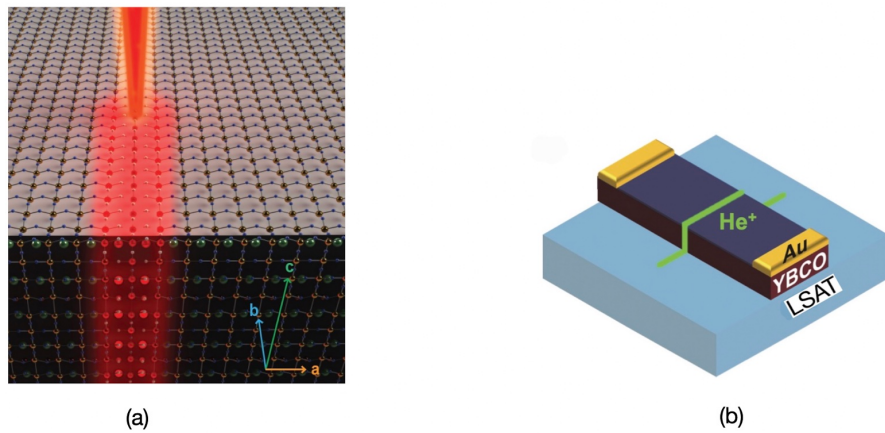


Figure 3.6: (a) Red line indicates focused He ion beam on atomic level with the width of the order of few nm order (b) Schematic sketch of the barrier JJ produced by He-FIB, the green line indicates the barrier JJ.

$$j_c(D) \approx j_{c,0} \exp(-D/D_0) \quad (3.1)$$

where  $j_{c,0}$  ( $\text{A}/\text{cm}^2$ ) and  $D_0$  (ions/nm) are the fitted critical current density at  $D=0$  and the character dose, respectively, obtaining by fitting experimental data using the eq. 3.1.

The BJJ's made by He-FIB can be changed continuously from conducting to completely insulating state by varying the irradiation dose. In fact, the He-FIB irradiation with high dose disturbs the internal atomic structure of YBCO, make irradiated line amorphous and highly resistive. It could play the role of resistive wall with  $j_c = 0$ .

We use this technique to structure ratchets that have more complex geometry than BJJs see the fig. 3.12.

## 3.5 Characterization

Before implementing the ratchet, we conducted a characterization of a series of BJJs with varying doses to determine the values of  $j_{c,0}$  and  $D_0$  for our specific chip. We fabricated 12 BJJs with dose series ranging between (450...700) ions/nm and subsequently measured the critical current of each junction. The results are presented in table. 3.1

BJJs	Dose (ion/nm)	Maximum $I_c$ ( $\mu\text{A}$ )
D19	455	15.6
D20	455	13.2
D21	505	11.5
D22	505	6.8
D23	556	1
D24	556	3.7
D25	606	1.4
D26	606	0.59
D27	657	0.17
D28	657	0.79
D29	707	0.29
D30	707	0.3

Table 3.1: The maximum  $I_c$  is determined by measuring  $I_c(H)$  and selecting the highest value, which may be reduced at  $I_{\text{coil}} \neq 0$ .

Next, we wrote a short python script to fit the experimental data using eq. (3.1) with  $j_{c,0}$  and  $D_0$  as fitting parameters. The result is shown in the fig. 3.7.

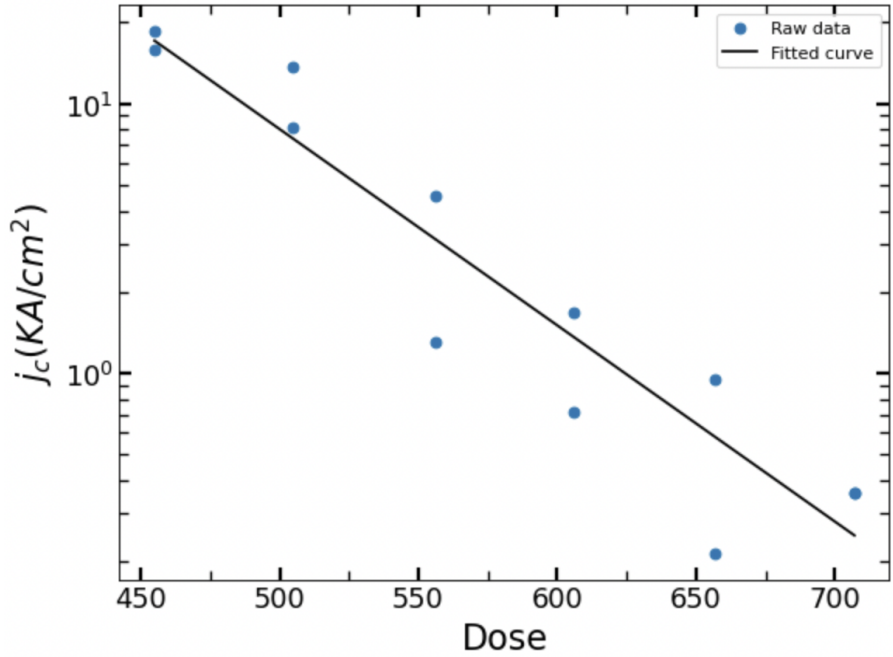


Figure 3.7: BJJs characterization  $j_c(D)$  experimental data and fit. 12 BJJs with the dose  $D = 450\dots700$  ion/nm. The width of the BJJs is  $2.8 \mu\text{m}$  and the film thickness is 30 nm.

As a result of fitting, we obtained  $j_{c,0} = 35\ 341\ 075.4 \text{ A}/\text{cm}^2$  and  $D_0 = 59.5 \text{ ion}/\text{nm}$ .

As an example, we present IVC and  $I_c(H)$  of several BJJs in fig. 3.8 to fig. 3.11.

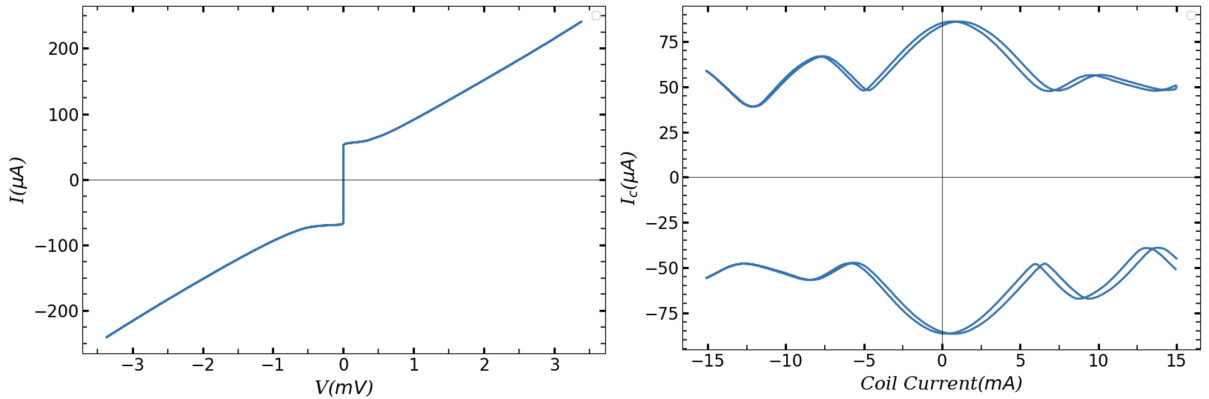


Figure 3.8: IVC and  $I_c(H)$  of junction B28 with dose 350 ion/nm.

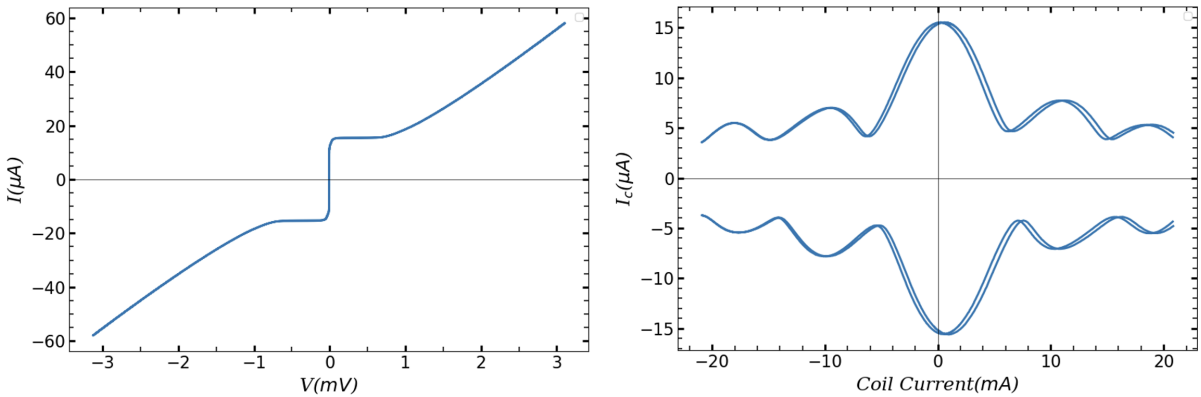


Figure 3.9: IVC and  $I_c(H)$  of junction D19 with dose 450 ion/nm.

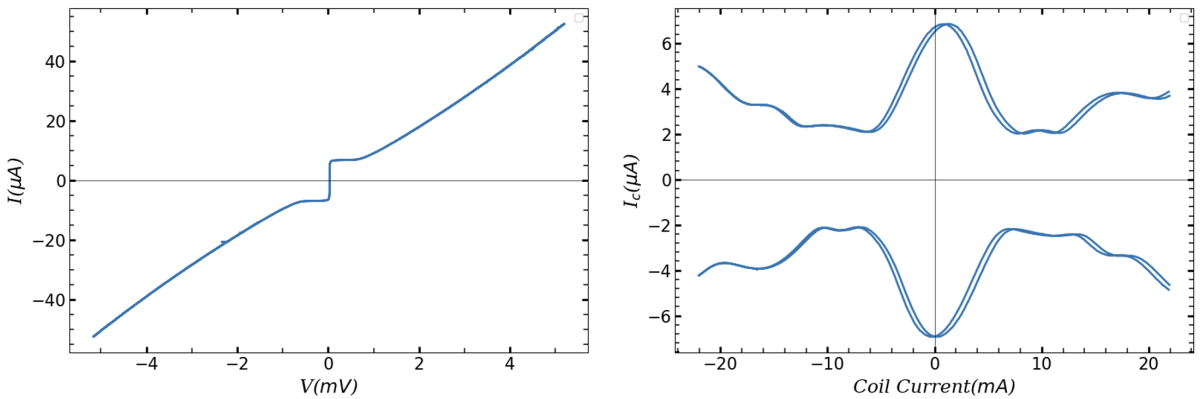


Figure 3.10: IVC and  $I_c(H)$  of junction D22 with dose 505 ion/nm.

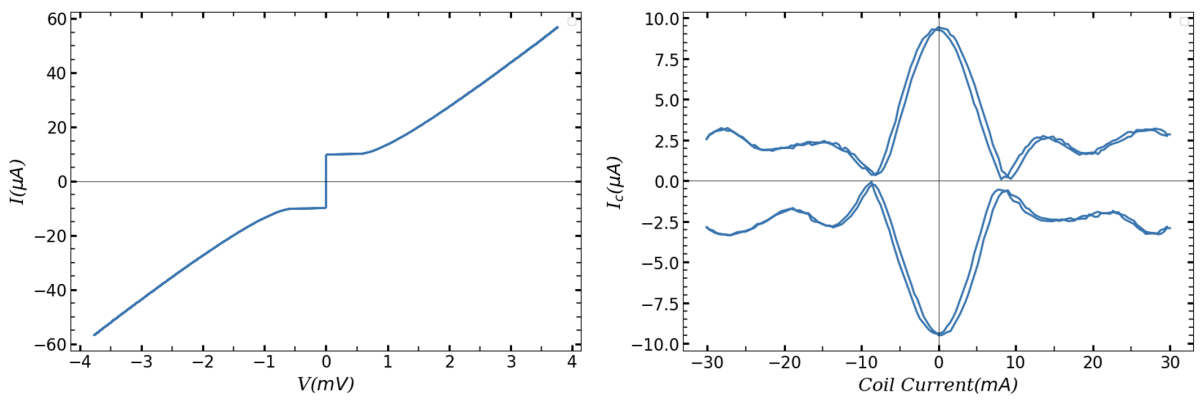


Figure 3.11: IVC and  $I_c(H)$  of junction B33 with dose 600 ion/nm.

## 3.6 Implementation of an In-line Geometry Josephson Ratchet

In-line geometry

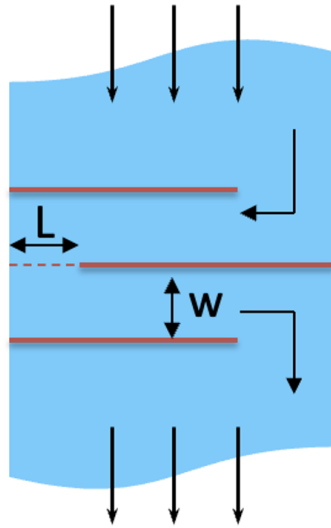


Figure 3.12: Sketch of a ratchet. The blue zone is YBCO, the red solid lines are the resistive wall, dash red line is the BJJ and arrows show the flow of the supercurrent.

In Chapter 2.1.3, we explored the impact of the in-line geometry of a Josephson junction (JJ) on the generation of a new magnetic field (self-field) within our device. This field is characterized by  $f^M$  and can be described by eq. (2.4). Additionally, we examined how this parameter influences the skewness of  $I_c(H)$  and, consequently, the asymmetry parameter. In this master thesis we focus on the implementation of a highly efficient ratchet based on reasonable theoretical parameters. For instance, eq. (2.4) clearly demonstrates the geometric dependencies of the ratchet on the length  $L$  of JJ and  $w$ . Therefore, we would design the ratchets with various values of  $f^M$ , while varying the length  $L$  of the JJ since  $L = \lambda_j \sqrt{4\pi f^M}$ . To optimize the the distance between two resistive walls  $w$ , we must avoid making it too small (less than or equal to 100 nm) to prevent the destruction of the crystal configuration of YBCO

due to resistive walls. Moreover, extremely small values of  $w$  can lead to the emergence of topological effects that might interfere with our desired parameters. Throughout this work, we refrain from reducing  $w$  below 200 nm.

Hence, our target parameters are selected as follows: after determining the desired value of the dimensionless parameter  $f^M$ , we fix the supercurrent density  $j_c(D)$  by adjusting the He-FIB irradiation dose using eq. (3.1). Subsequently, we can obtain the Josephson penetration depth  $\lambda_j$  and determine the appropriate length  $L$  using eq. (2.4), and then we can find the critical density by  $I_c = j_c \cdot L \cdot t$  where  $t$  in our case is 30 nm. By following this approach, we can theoretically estimate all the parameters required for our ratchet. In the table 3.2, we present the sets of target parameters for ratchets A15 and A22, which will be discussed in detail later.

Target Parameters	A15	A22
$w(\text{nm})$	300	200
Dose(ion/nm)	507	531
$j_c (\text{kA}/\text{cm}^2)$	7.04	4.7
$I_c(\mu\text{A})$	3.7	2.5
$\lambda_j(\text{nm})$	356	353
$L(\text{nm})$	1750	1750
$l \equiv L/\lambda_j$	4.9	4.9
$f^M$	1.9	1.9

Table 3.2: Comparison table of target parameters between ratchet A15 and A22.

# Chapter 4

## Experimental Results

### 4.1 An Overview

In this chapter, we report the set of experimental results for the ratchets A22 and A15. First we compare the actual (experimental) and target (theoretical) parameters of each devices, then we will present our experimental data for the set of measurements, including IVC,  $I_c(H)$ ,  $\bar{V}_{dc}$ ,  $\bar{P}_{out}$ ,  $\bar{P}_{in}$ , and finally, the efficiency  $\eta$ . We will then compare our experimental results with the figures of merit of our ratchets, which are simulated in the quasistatic regime. Finally, we will drive our system with stochastic drive (Gaussian drive) and investigate the effect of different type of noises such as external and thermal noises. It is shown how the noises due to thermal sources can be rectified into the output dc voltage.

### 4.2 Ratchet A22

In the table. 4.1, the actual and target parameters of the device A22 are presented.

A22	Target parameter	Actual parameter
$w$ (nm)	200	200
Dose(ion/nm)	531	531
$j_c$ (kA/cm <sup>2</sup> )	4.7	28
$I_c$ ( $\mu$ A)	2.5	14.8
$\lambda_j$ (nm)	353	145
$L$ (nm)	1750	1750
$l_j \equiv L/\lambda_j$	4.9	12
$f^M$	2	11.6

Table 4.1: Comparison table of target and actual parameters of ratchet A22.

The target and actual parameters for the length  $L$  and  $w$  are fixed to the same values. The differences in  $j_c$  are approximately six order of magnitude, which can be attributed to the inherent spread of our technology He-FIB. However, this variance has resulted in the fabrication of highly efficient BJJs. Consequently, the differences in  $I_c$  align with the order of magnitude difference in  $j_c$ . In general, discrepancies between the actual and target parameters can arise due to various factors such as fabrication techniques, lithography processes, and other measurement procedures. The IVC and  $I_c(I_{coil})$  of the ratchet A22 are presented in figs. 4.1 and 4.2, respectively.

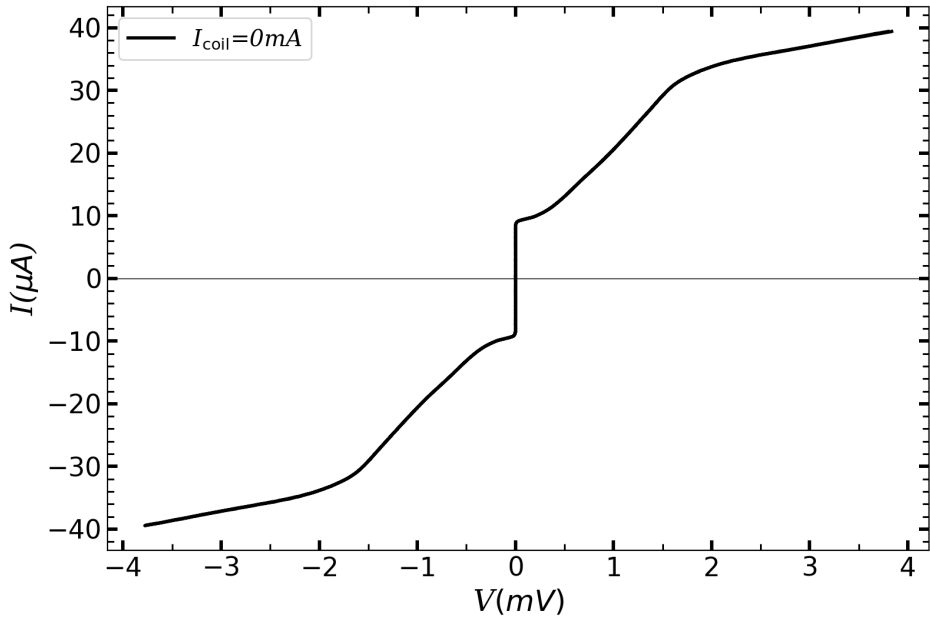


Figure 4.1: IVC of the ratchet A22 at  $I_{\text{coil}} = 0 \text{ mA}$  where  $|I_{c+}| \approx |I_{c-}| \approx 8.43 \mu\text{A}$ .

The internal resistance of our ratchet system, as indicated in the fig. 4.1, is approximately  $R_N \approx 50 \Omega$ . It is worth noting that the observed bending near  $|I_+| \approx |I_-| \approx 30 \mu\text{A}$  may stem from the choice of a slightly shorter distance between the two resistive walls  $w$ . Consequently, it is possible that some crystal destruction of YBCO has already occurred, leading to this bending phenomenon. However, it is important to acknowledge that the exact cause cannot be determined with absolute certainty.

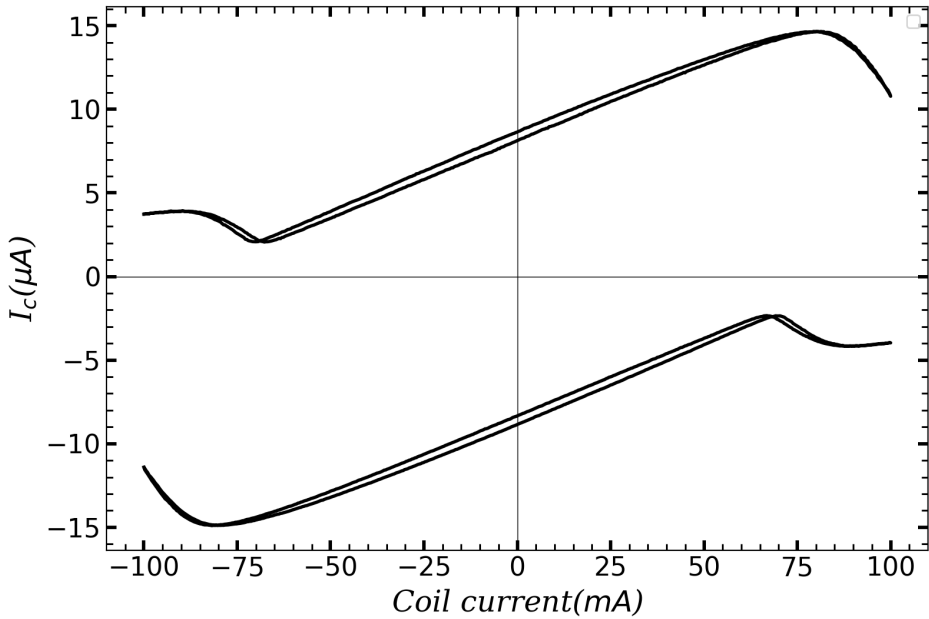


Figure 4.2: Critical current versus magnetic coil current of the ratchet A22. We used a voltage criterion equal to  $1 \mu\text{V}$  for this measurement.

Our coil current range is between (-100...+100) mA, we can clearly observe the skewed nature of  $I_c(I_{\text{coil}})$ . Using the fig. 4.2, we can identify the optimal magnetic field for which the asymmetry parameter  $\mathcal{A}$  is at its maximum. This will enable us to apply the optimal magnetic field to our device and obtain an asymmetric IVC. To determine the dependence of asymmetry parameters, eq. (2.1), on the coil current  $\mathcal{A}(I_{\text{coil}})$ , we have written a Python script which the resulting depend on  $\mathcal{A}(I_{\text{coil}})$  is shown in fig. 4.3.

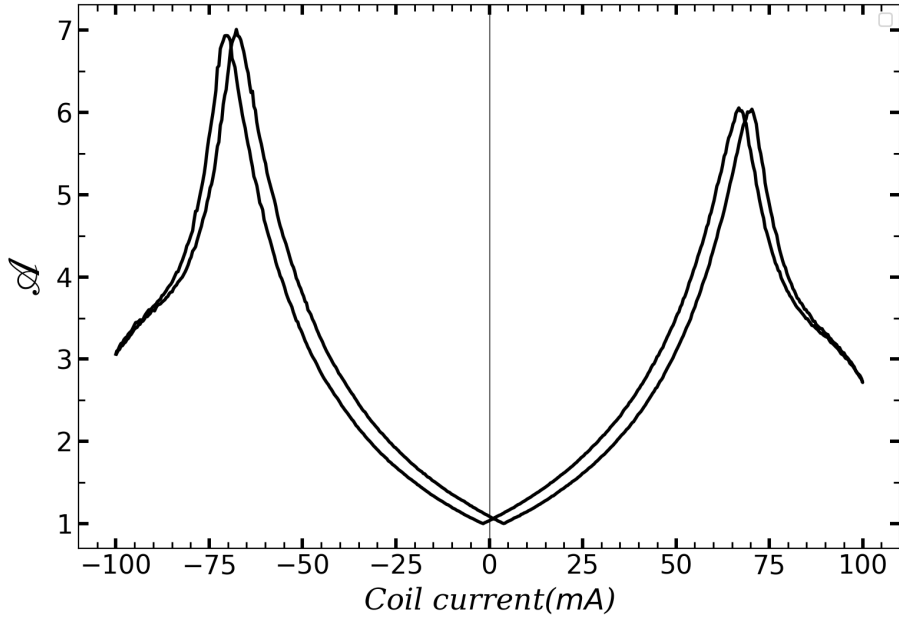


Figure 4.3: Value of asymmetry parameter, which shows the maximum asymmetry, is  $\mathcal{A} \approx 7$  at the value of  $I_{\text{coil}} = -69$  mA.

We have observed that  $\mathcal{A}$  is somewhat asymmetric with respect to polarity of  $I_{\text{coil}}$ . For instance, for  $I_{\text{coil}} = 69$  mA,  $\mathcal{A}(69\text{ mA}) \approx 6$  whereas for  $\mathcal{A}(-69\text{ mA}) \approx 7$ . This asymmetry can be attributed to several factors; such as the shift of zero for the current source used to bias the JJ or the design of our ratchet itself. (For instance, if the lengths of the two resistive walls shown in fig. 3.11 are not precisely same, then such small differences and offsets of the optimum point in  $\mathcal{A}$  for different polarities of current would be expected. NOT SURE ABOUT THIS STATEMENT, ITS NOT CORRECT, RIGHT?)

Another issue, which we want to point out, concerns the discrepancy between the theoretically predicted  $\mathcal{A} \approx 400$  and the experimental results  $\mathcal{A} \approx 7$ . As we briefly mentioned in page. 26, this difference is mainly due to our choice of voltage criterion and many possible noise sources. These two main reasons causes the  $I_c$  at the optimum point in fig. 4.2 not to be close to zero, and therefore,  $\mathcal{A}$  does not

close to its theoretical prediction,  $\mathcal{A} \approx 400$ . For example, if we could reduce the thermal and other external source of noises, the  $I_{c-}$  in the optimum point would be much closer to zero. Thus, the value of  $\mathcal{A}$  would be much closer to its theoretical prediction. Therefore, looking at fig. 4.3, the important point for us is to find the optimum  $I_{\text{coil}}$  where  $\mathcal{A}$  has a maximum. Once we find the magnetic optimum field, we can apply it across our device to capture the experimental asymmetric IVC. After obtaining the asymmetric IVC as shown in the fig. 4.4, we can proceed to measure all the other parameters and conduct further measurements.

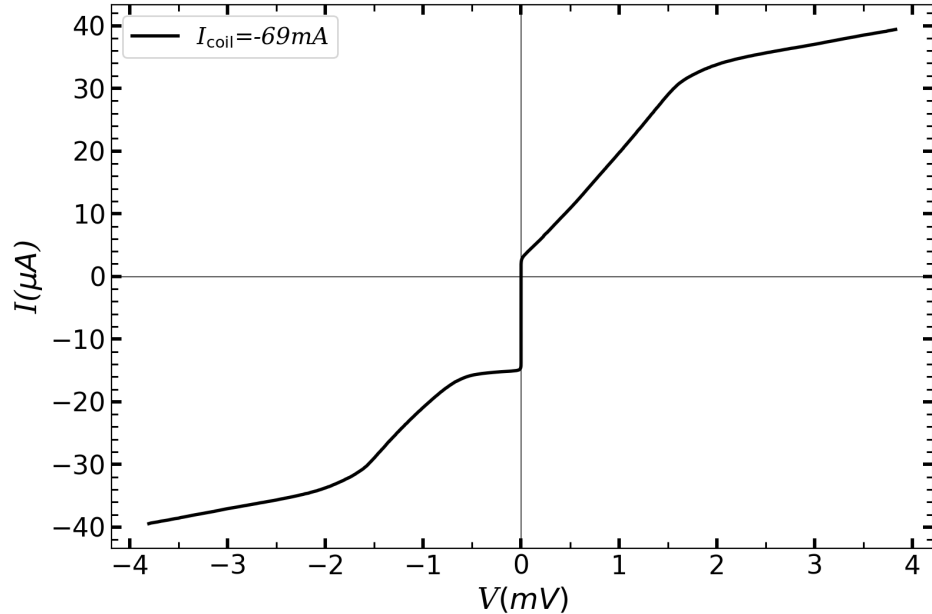


Figure 4.4: IVC of the ratchet A22 at the optimum magnetic field (coil current)  $I_{\text{coil}} = -69 \text{ mA}$  exhibits  $|I_{c+}| \approx 1.53 \mu\text{A}$  and  $|I_{c-}| \approx -13.8 \mu\text{A}$  that makes  $\mathcal{A} \approx 7$ .

Having such an asymmetric IVC we can now apply some ac-drive  $I(t) = I_{\text{ac}} \sin \omega t$  and measure the rectification curve  $\bar{V}_{\text{dc}}(I_{\text{ac}})$  as follow,

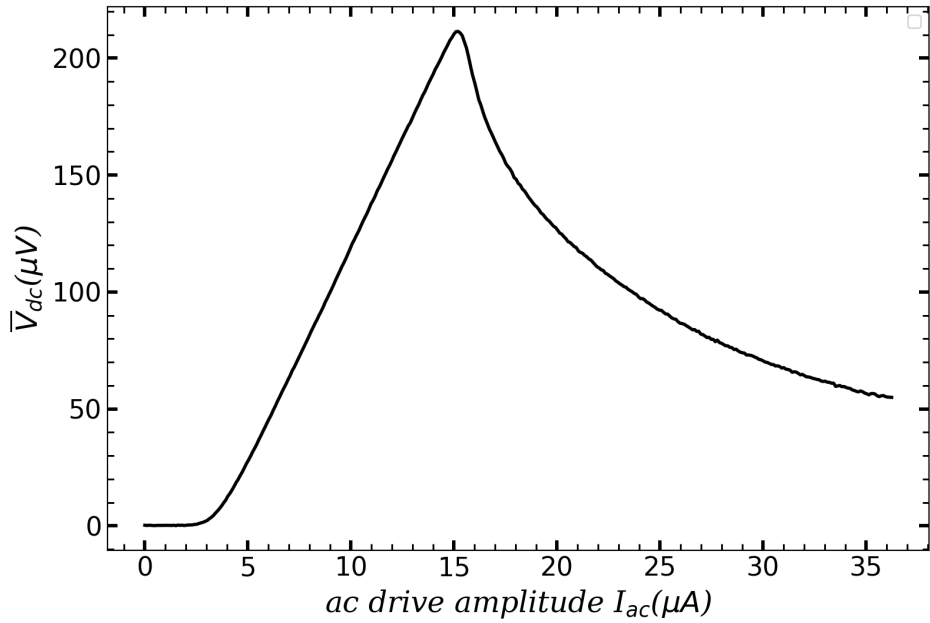


Figure 4.5: The rectification curve for the ratchet A22 at  $I_{\text{coil}} = -69 \text{ mA}$  where  $|I_{c-}| \approx 15.2 \mu\text{A}$ ,  $|I_{c+}| \approx 2.2 \mu\text{A}$  and RW  $\Delta \approx 13 \mu\text{A}$ .

The rectification curve is experimentally measured and shown in the fig 4.5. For short amplitude of ac-drive the particle does not move and  $\bar{V}_{dc}$  remains zero until the ac-drive amplitude reaches approximately  $|I_{c+}| \approx 2.2 \mu\text{A}$ . From that point onwards, the particle starts moving, rectification occurs, and the particle reaches its maximum velocity when the ac-drive amplitude reaches approximately  $|I_{c-}| \approx 15.2 \mu\text{A}$  where the maximum  $\bar{V}_{dc}(I(t)) \approx 213 \mu\text{V}$ . As the ac-amplitude increases further, the average velocity slowly decreases. However, our ratchet is still idle. To make it not idle, we will load it by applying some counterforces ( $I_{dc}$ ) in the opposite direction of the ratchet motion to compel the particle to climb uphill and generate some useful work. The rectification curve, depicting the loaded state for different values of  $I_{dc}$ , is shown in fig. 4.6,

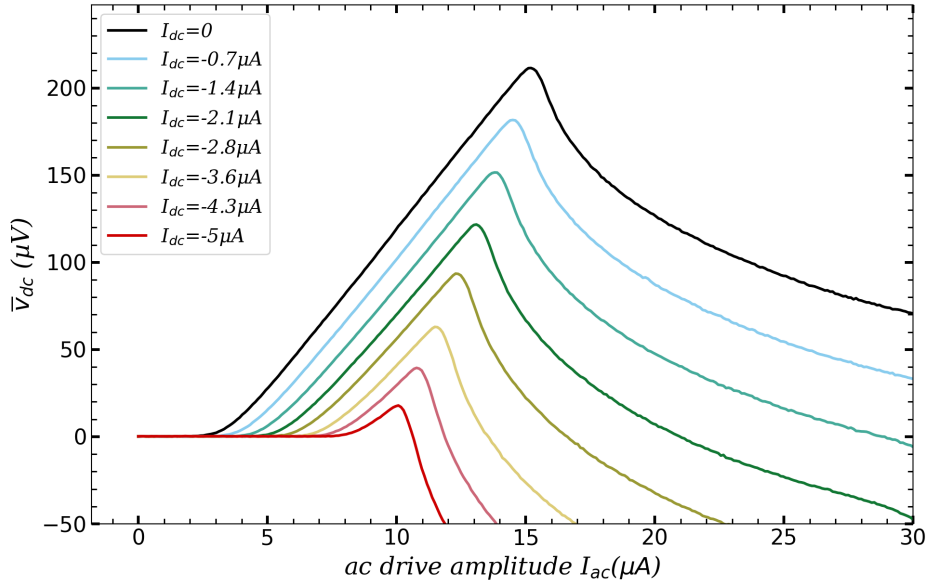


Figure 4.6: The rectification curve for the ratchet A22 at  $I_{\text{coil}} = -69 \text{ mA}$  for several  $I_{\text{dc}}$  up to  $|I_{\text{dc}}| = 5 \mu \text{A}$ .

We observe that by increasing absolute value of the counterforce, the RW shrinks until it closes at the stopping force around  $|I_{\text{dc}}| \approx 5 \mu \text{A}$ . After that, the the particle gradually stops moving and  $\bar{V}_{\text{dc}}(I(t)) = 0$ . It is interesting to mention that in the study conducted by [3], the authors derived the theoretical value of  $I_{\text{stop}}$  as  $I_{\text{stop}} = \frac{|I_c_-| - |I_{c+}|}{2}$ . In our case, we obtained a value of approximately  $-6.1 \mu \text{A}$  for  $I_{\text{stop}}$ , which closely aligns with our experimental finding of around  $-5.5 \mu \text{A}$ .

Now we can move on to measure the output power  $\bar{P}_{\text{out}}$  by multiplying  $\bar{V}_{\text{dc}}(I(t))$  with different values of  $I_{\text{dc}}$  as e.g.  $\bar{P}_{\text{out}} = \langle VI((t)) \times I_{\text{dc}} \rangle = \bar{V}_{\text{dc}} \cdot I_{\text{dc}}$ . Then we measure the input power  $\bar{P}_{\text{in}} = \langle V(I(t)) \times I(t) \rangle$  for the applied ac-drive. And finally, The efficiency from our experimental data is calculated. The values of  $\bar{P}_{\text{in}}$ ,  $\bar{P}_{\text{out}}$ , and  $\eta$  respectively are given by fig. 4.7,

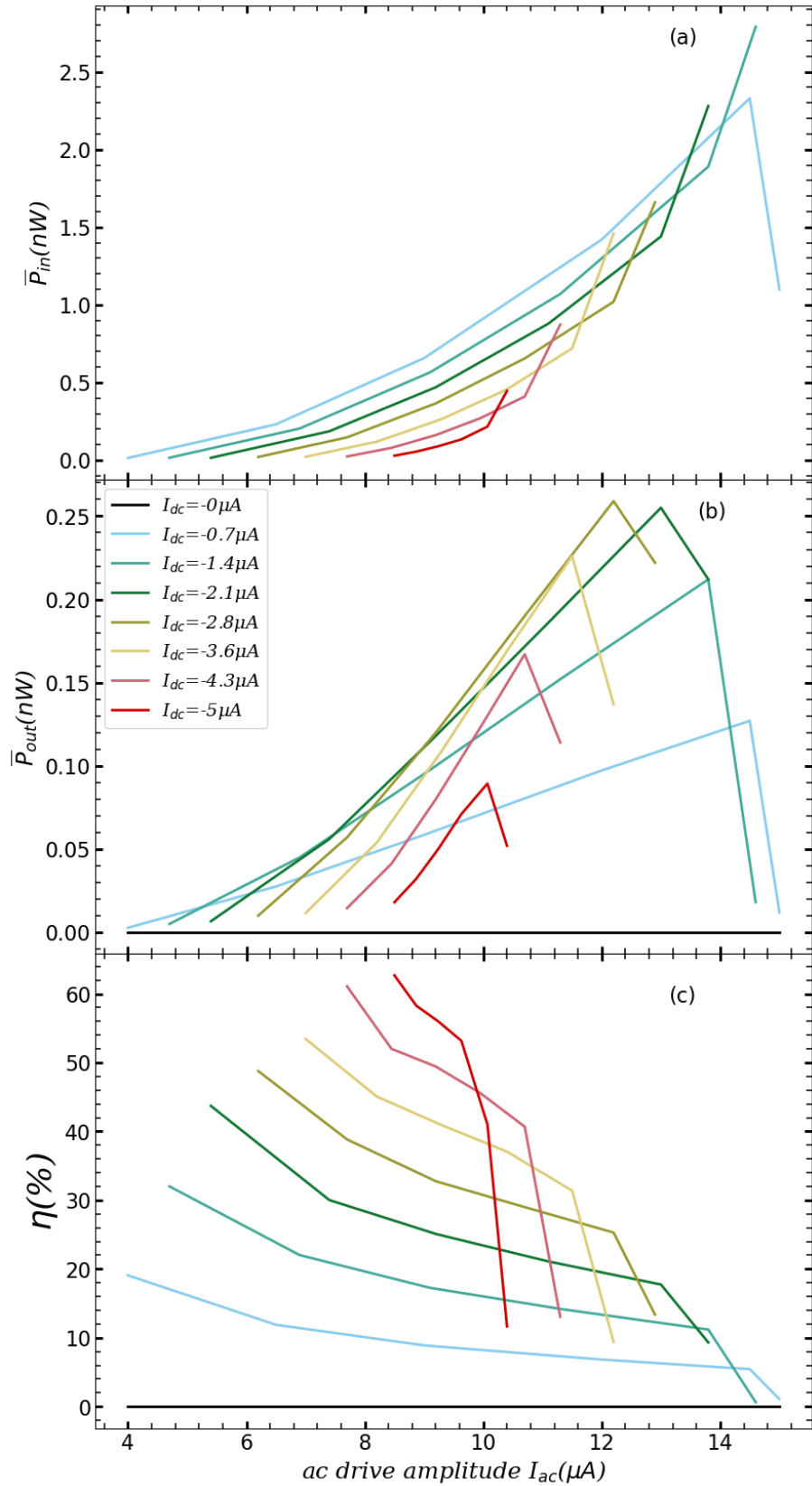


Figure 4.7: (a)  $\overline{P}_{in}$ , (b)  $\overline{P}_{out}$ , (c) efficiency  $\eta$ .

To measure  $\bar{P}_{\text{out}}$  we just simply multiply each  $\bar{V}_{\text{dc}}$  value by its corresponding  $I_{\text{dc}}$ . However, measuring  $\bar{P}_{\text{in}}$  presented a slightly more challenging situation as we were unable to pull  $I(t)$  out of the average and integral. Therefore, we divided the operation interval (RW) for each curves in the fig. 4.6 into six intervals of ac amplitude. Within each interval, we measured  $V(I(t))$  and then summed up the obtained  $V$  values to obtain a single experimental data point. Therefore, in total, we measured  $V$  for 42 times which leads to 42 points in  $\bar{P}_{\text{in}}$ .

In the fig. 4.7(b), we observe that increasing  $I_{\text{dc}}$  leads to an increase in  $\bar{P}_{\text{out}}$  until  $I_{\text{dc}} = -2.8 \mu\text{A}$ . Further increases in  $I_{\text{dc}}$  cause a decrease in  $\bar{P}_{\text{out}}$ .

For efficiency fig. 4.7(c), we first observe that unlike  $\bar{P}_{\text{out}}$ , efficiency constantly increases by growing the values of  $I_{\text{dc}}$ , while the RW decreases. Furthermore, we note that for every values of  $I_{\text{dc}}$ , the maximum efficiency occurs at the beginning of the RWs, aligning with the predictions and simulations presented in Chapter 2.

In the next subsection, we will present the simulation results of the ratchet A22 and compare them with its corresponding experimental data.

#### 4.2.1 Experimental Simulation of A22

In the quasistatic regime, one can simulate all the interested figures of merit by using the asymmetric IVC as a reference input and then generating all the other parameters, namely  $\bar{V}_{dc}$ ,  $\bar{P}_{in}$ ,  $\bar{P}_{out}$ , and  $\eta$ . These figures of merit are presented in the fig. 4.8 and 4.9, and are compared with the experimental data simultaneously.

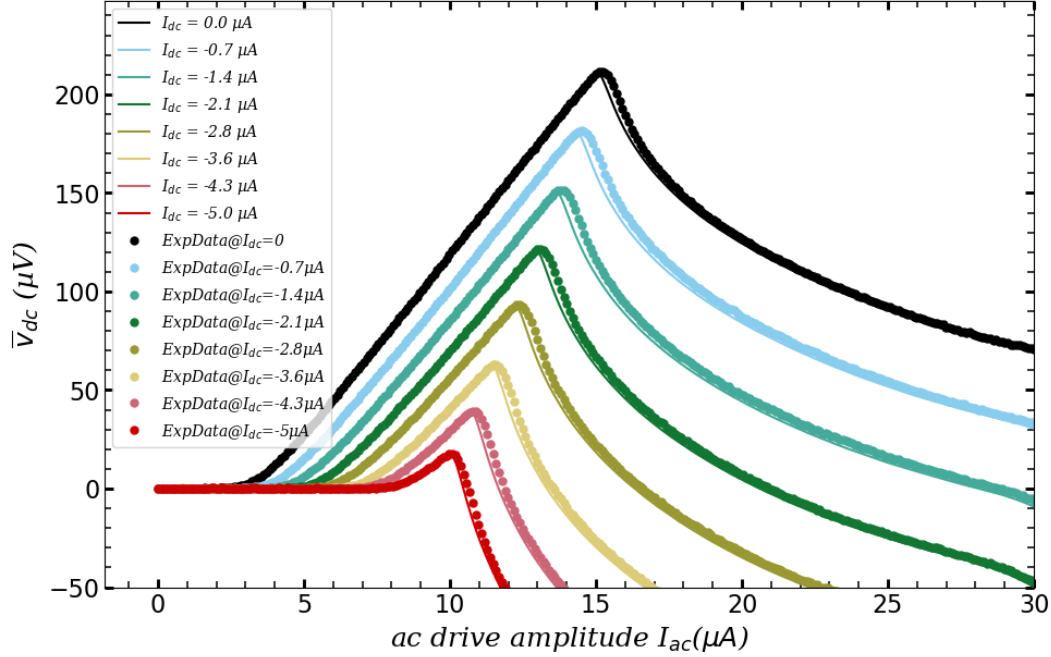


Figure 4.8: Simulations (lines) versus the experimental data (dots) of  $\bar{V}_{dc}(I(t))$

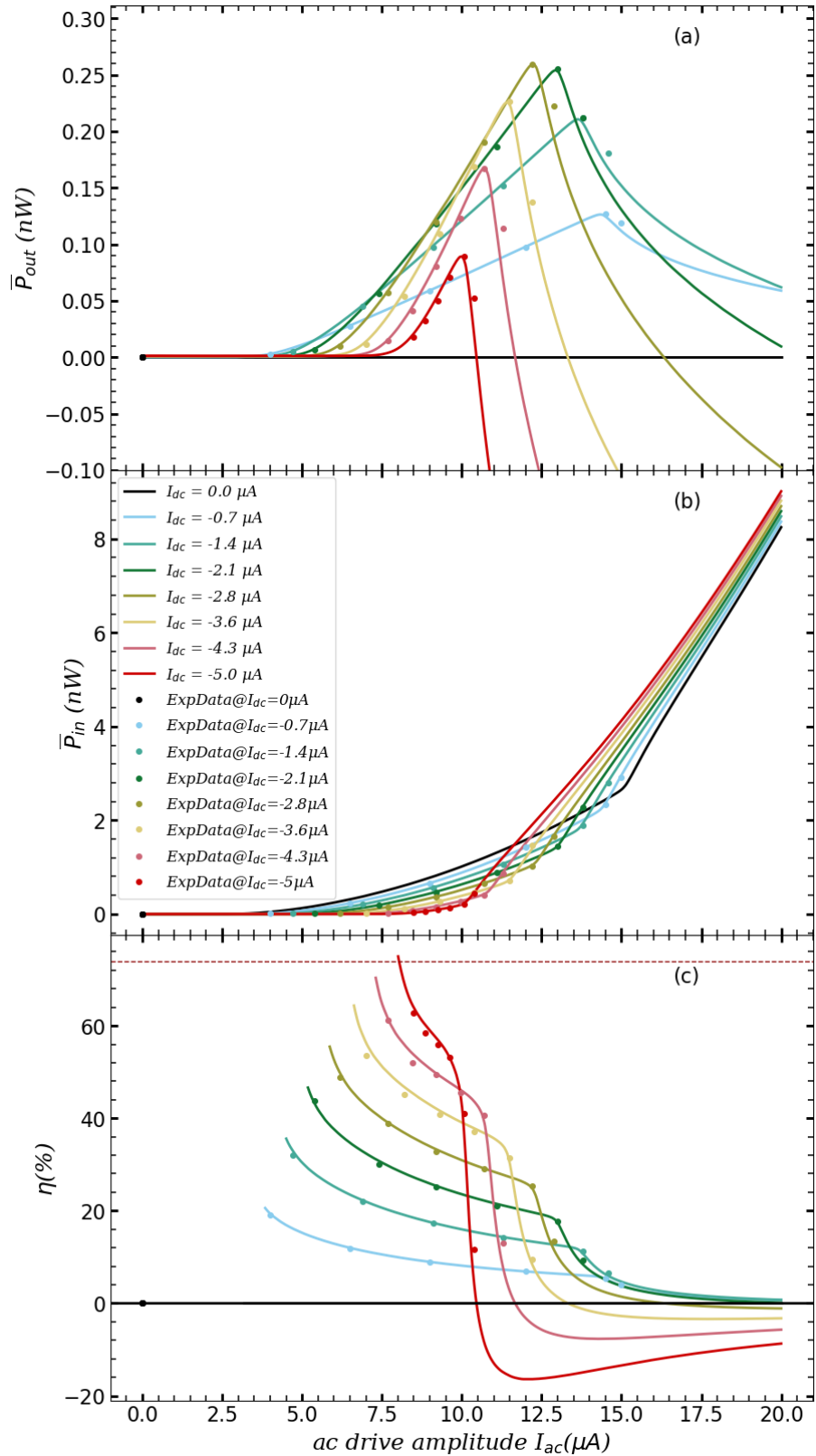


Figure 4.9: Simulations (lines) versus the experimental data (dots) of (a)  $\bar{P}_{\text{in}}$ , (b)  $\bar{P}_{\text{out}}$ , and (c)  $\eta$ .

Clearly, we observe that our experimental data are well fitted by our simulation results and the figures of merit. It is enlightening to mention that the theoretical maximum efficiency calculated in [3] (red dashed line in the fig. 4.9(c)) is around 74% which is nicely touches our maximum simulation curve.

### 4.3 Ratchet A15

In this section, we will present the set of parameters for ratchet A15, similar to the previous section. A comparison between the actual and target parameters is provided in Table 4.2

A15	Target parameter	Actual parameter
$w(\text{nm})$	300	300
Dose(ion/nm)	507	507
$j_c (\text{kA}/\text{cm}^2)$	0.7	53
$I_c(\mu\text{A})$	3.7	28
$\lambda_j(\text{nm})$	129	356
$L(\text{nm})$	1750	1750
$l \equiv L/\lambda_j$	4.9	13.5
$f^M$	1.47	14.6

Table 4.2: Comparison table of target and actual parameters of ratchet A15

In the following the IVC and  $I_c(H)$  of the ratchet A15 are presented,

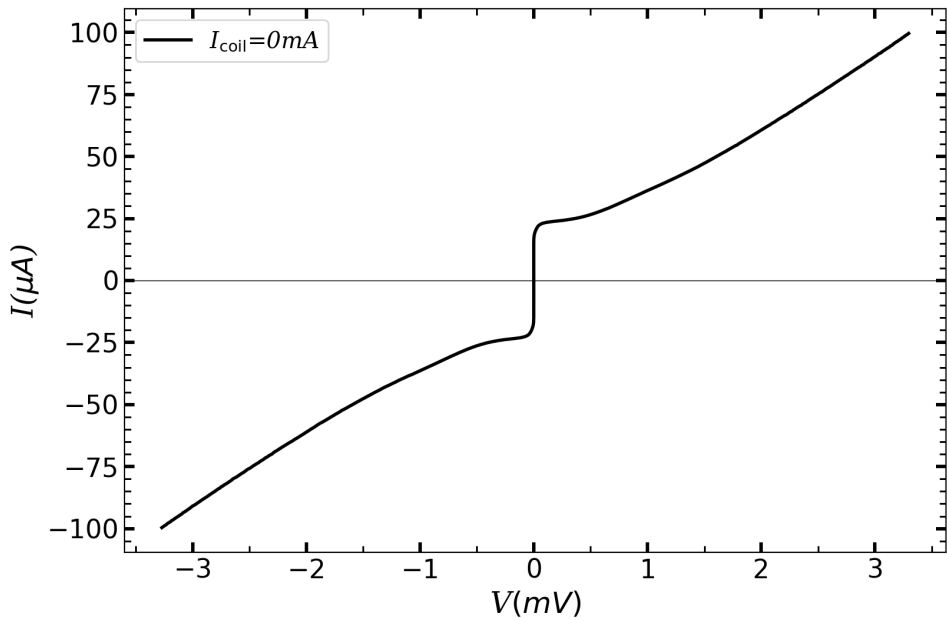


Figure 4.10: IVC of the ratchet A15 at  $I_{\text{coil}} = 0$ .  $|I_{c+}| = |I_{c-}| \approx 21 \mu\text{A}$  and  $R_N \approx 32 \Omega$ .

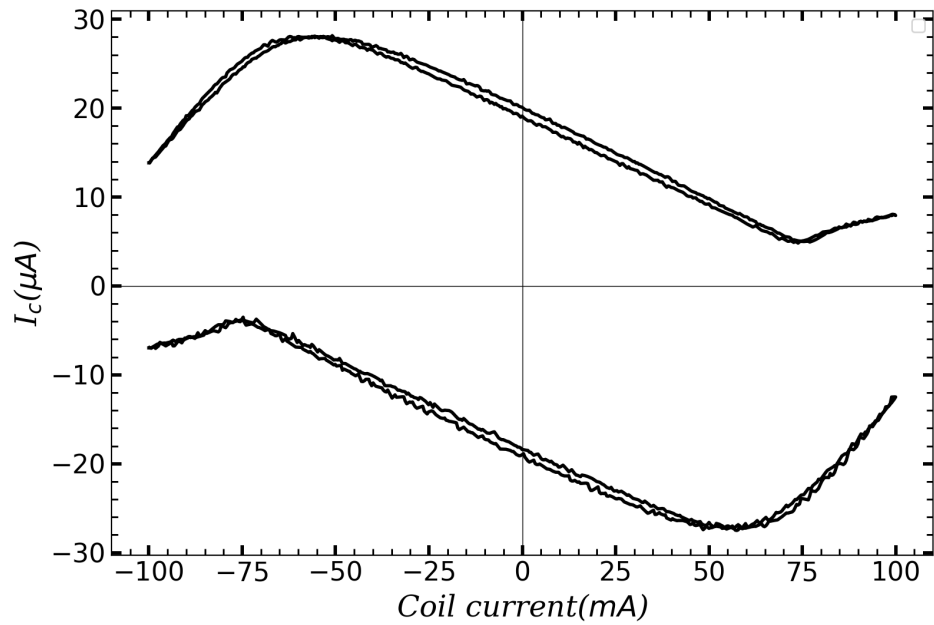


Figure 4.11: Critical current versus magnetic coil current of the ratchet A15

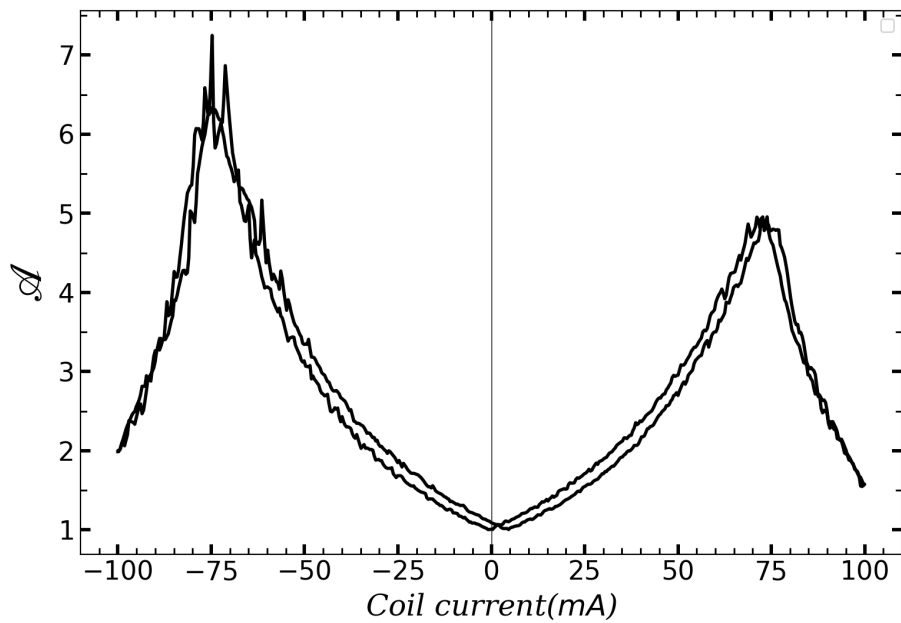


Figure 4.12: The value of asymmetry parameter which shows the maximum asymmetry  $\mathcal{A} \approx 7$  at optimum magnetic  $I_{\text{coil}} = 75$  mA.

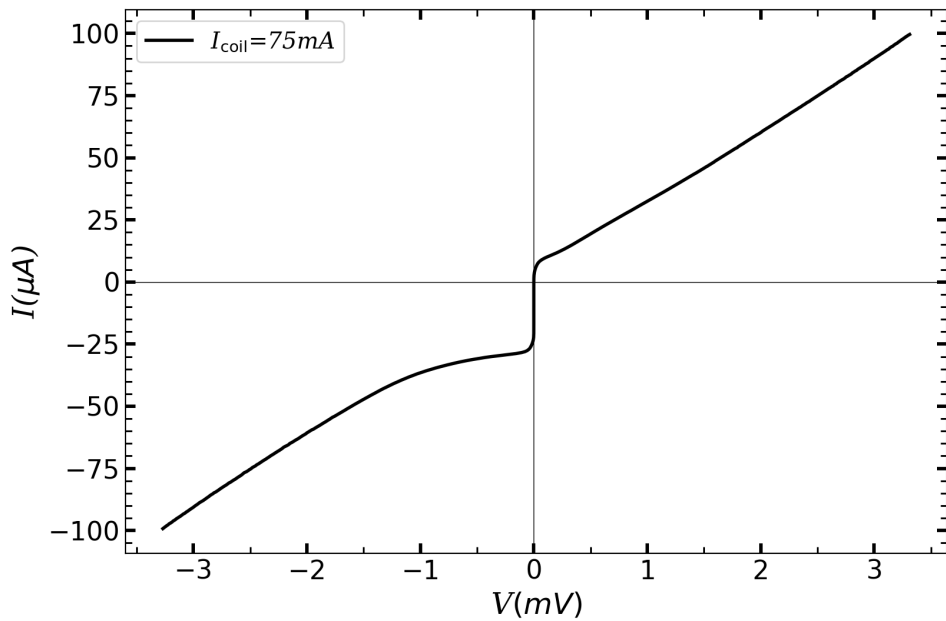


Figure 4.13: An asymmetric IVC of the ratchet A15 at the optimum  $I_{\text{coil}} = 75$  mA has  $|I_{c-}| \approx 24.5 \mu\text{A}$  and  $|I_{c+}| \approx 3.5 \mu\text{A}$ .

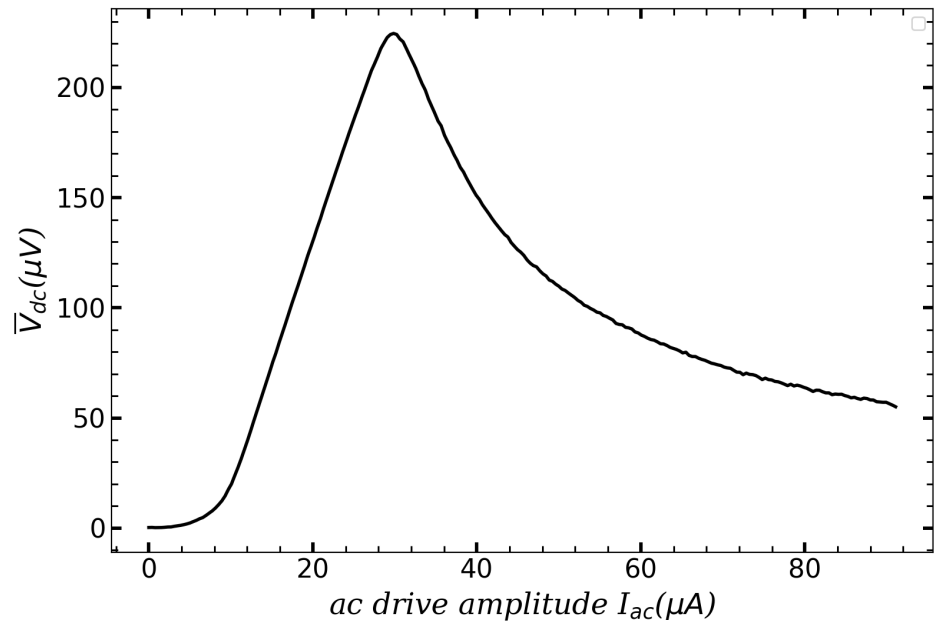


Figure 4.14: The rectification curve for the ratchet A15 at  $I_{\text{coil}} = 75 \text{ mA}$ .

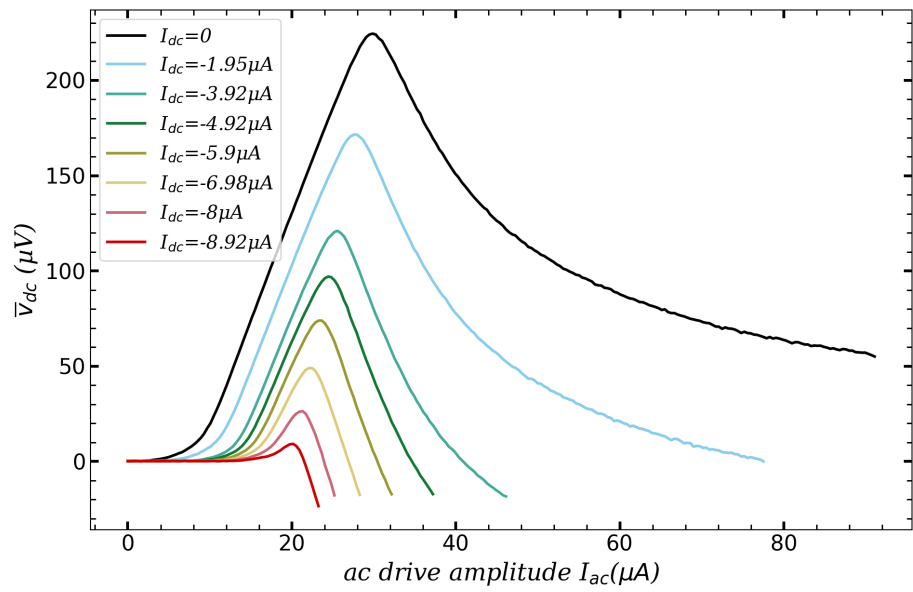
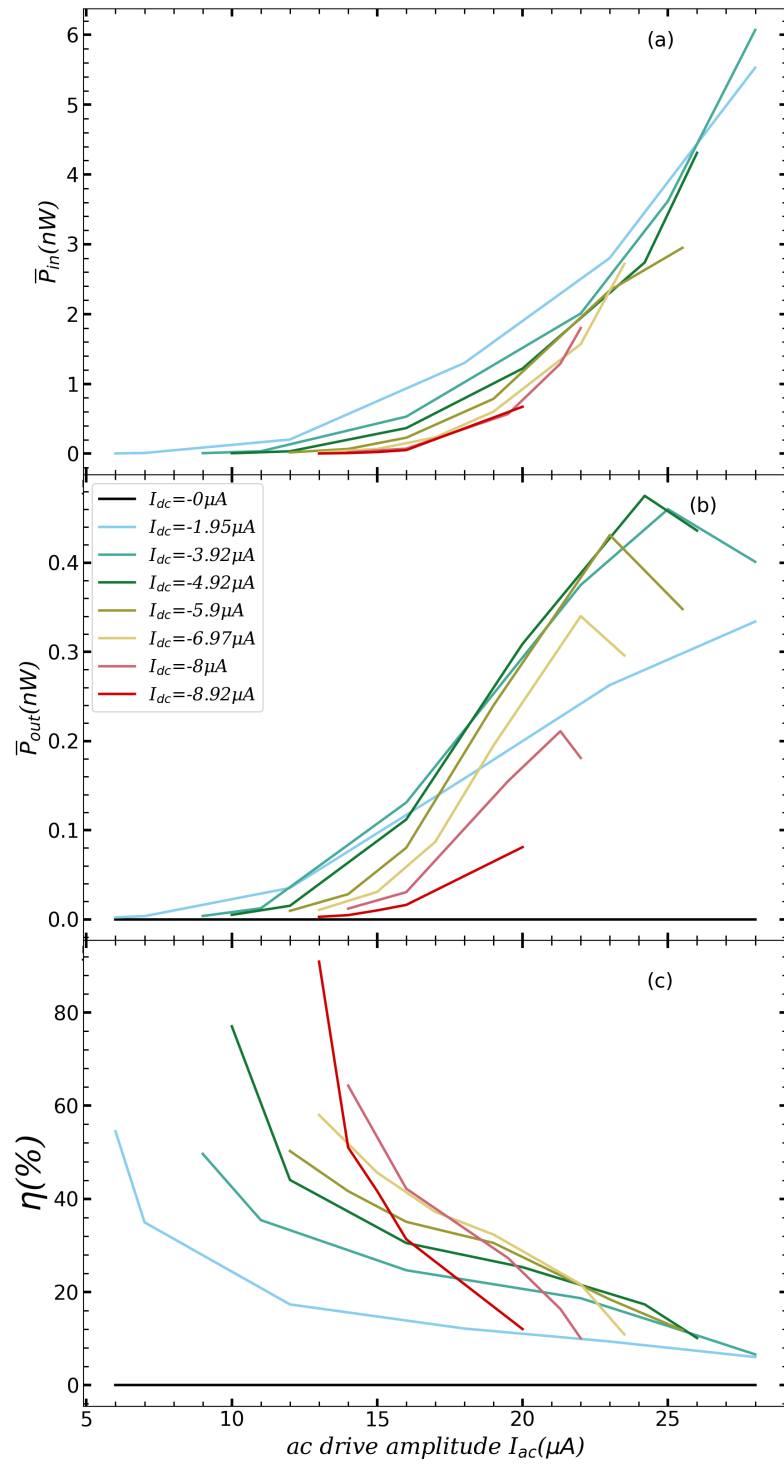


Figure 4.15: The rectification curve for the ratchet A15 at  $I_{\text{coil}} = 75 \text{ mA}$  for several  $I_{\text{dc}}$  up to  $|I_{\text{dc}}| = 8.92 \mu\text{A}$ .



## 4.4 Driving the Ratchet with a Stochastic Signal

In this section, our objective is to examine the influence of different types of noise on the system and assess their impact on precision. In reality, numerous sources of noise can affect the system and diminish its accuracy. Therefore, we explore two distinct approaches: external and internal noises. Both approaches incorporate the utilization of random normal noise, which adheres to a Gaussian distribution. A schematic representation of the stochastic signal and its corresponding distribution can be found in the fig. 4.17,

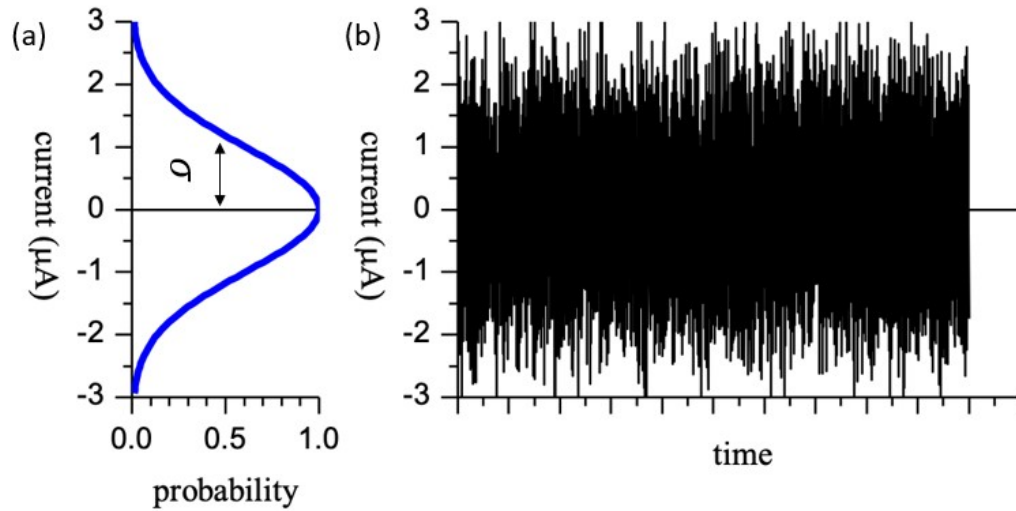


Figure 4.17: (a) The Gaussian distribution of random signal with the width  $\sigma$  (b) The random signal depends on time.

#### 4.4.1 External noise

For the first case, our focus is on examining the impact of external noises by simulation. To accomplish this, we substitute the deterministic ac-drive with an external random signal to drive the ratchet system in a stochastic regime. Given that we are operating in the quasistatic regime, we can once again consider an asymmetric IVC of A22 and simulate all the figures of merit by driving the system with the Gaussian signal. It is important to note that the amplitude of the Gaussian signal is infinite and random. Therefore, we adopt the parameter  $\sigma$  as a measure of the amplitude of our noisy signal. The simulated  $\bar{V}_{dc}$ ,  $\bar{P}_{in}$ ,  $\bar{P}_{out}$ , and efficiency  $\eta$  are presented in the fig. 4.18 and fig. 4.19,

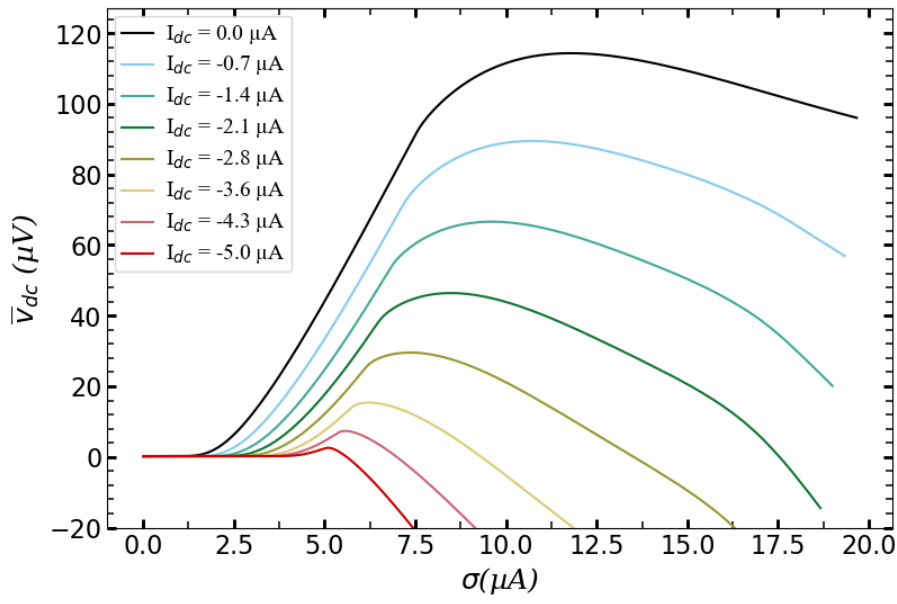


Figure 4.18: Simulation of  $\bar{V}_{dc}$  drive with Gaussian signal.

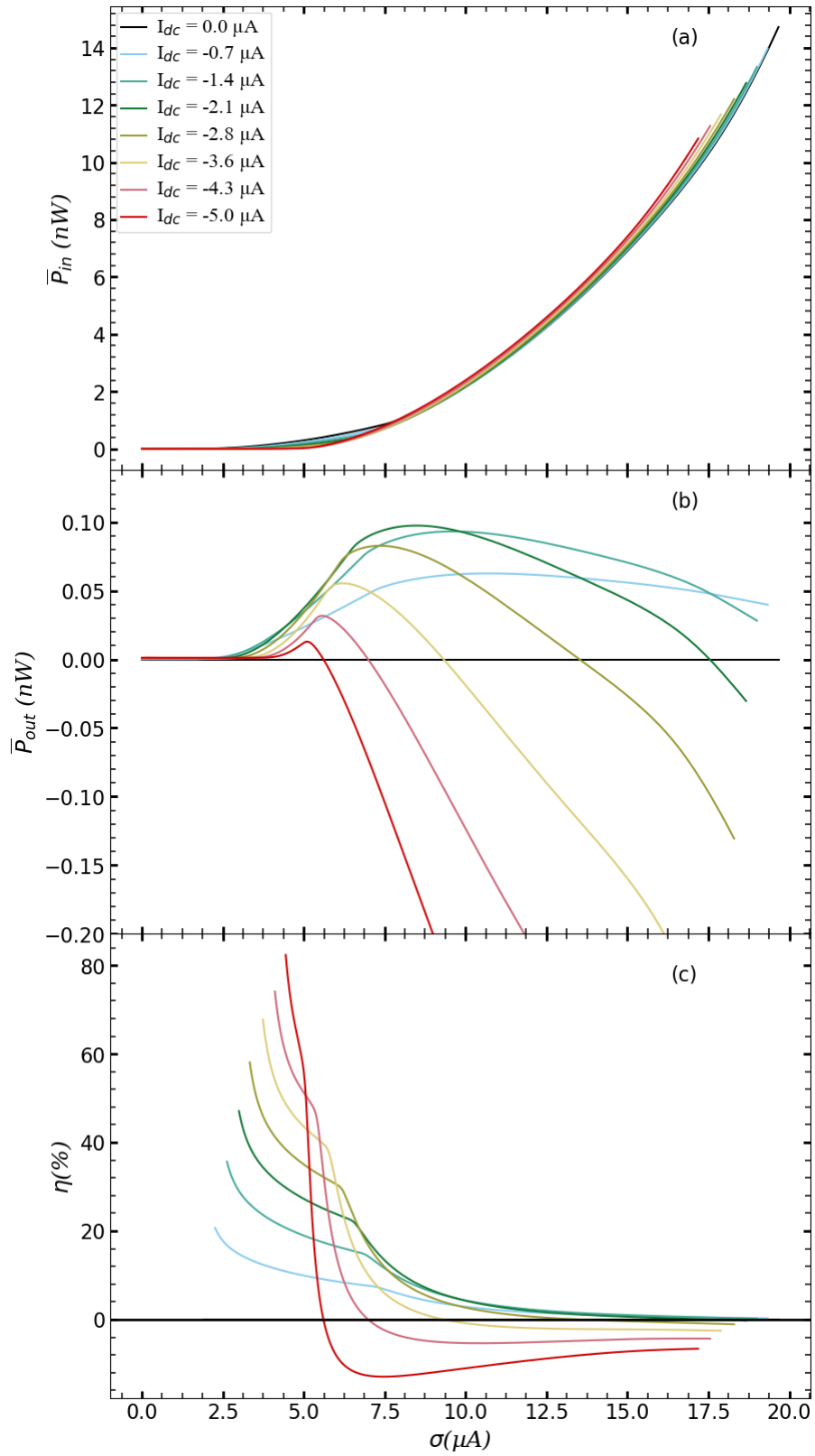


Figure 4.19: (a)  $\bar{P}_{in}$ , (b)  $\bar{P}_{out}$ , (c) and  $\eta$

In conclusion, we observe that our ratchet system remains functional when driven by a random signal instead of a deterministic drive. The figures of merit obtained under the random signal exhibit a similar behavior to those achieved under the deterministic drive. However, it is worth noting that the maximum value of the average voltage  $\bar{V}_{dc}$ , decreases by a factor of two compared to deterministic drive (ac-drive). Thus, in principle, we drive the system with noise and observe that the noise can also facilitate the transfer of the particle, albeit at a slower pace.

#### 4.4.2 Internal noise

For the case of internal noise, we utilize the inherent noise present within the system, commonly referred to as thermal noise. Thermal noise arises from the random fluctuations resulting from the thermal energy of the system, specifically in the shunt resistor at a finite temperature. These fluctuations exhibit an amplitude distribution that is nearly Gaussian. The fluctuation-dissipation theorem provides a generic and statistically derived explanation for this phenomenon in the field of statistical physics.

Due to the utilization of high-temperature superconductors (HTSs), our ratchet system can be operated at temperatures up to 40K. At this temperature, the thermal energy ( $k_B T$ ) is approximately ten times greater compared to when the temperature is 4K. Consequently, the ratchet can be operated with a significantly higher thermal energy level. In the following we present the IVC of the ratchet A15 at temperature around 4.2K and 35K.

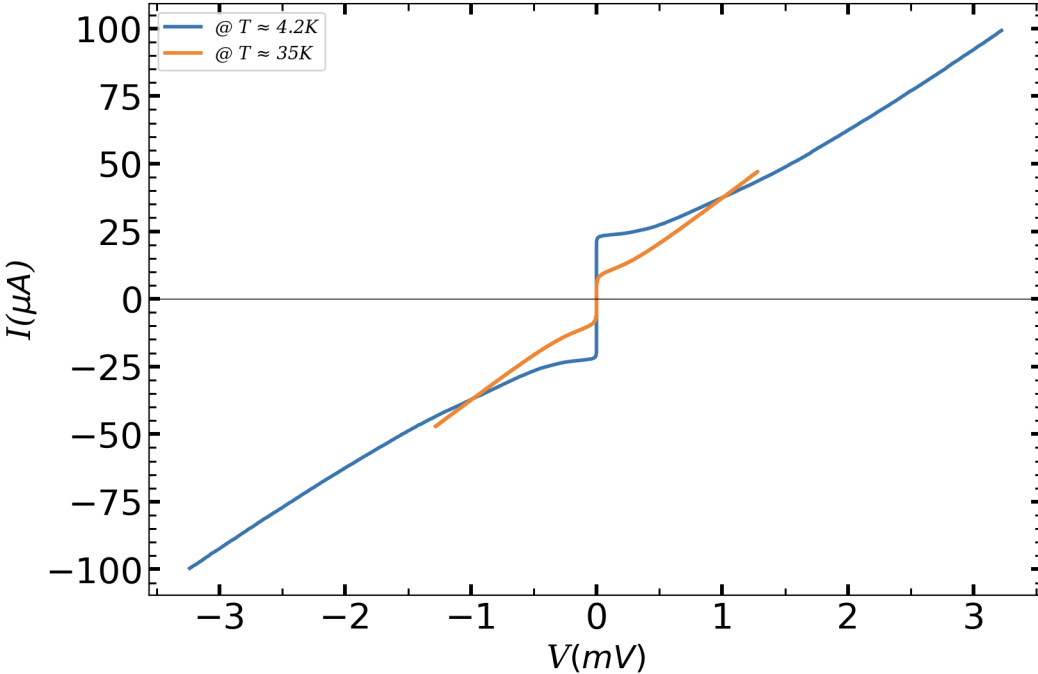


Figure 4.20: IVC of A15 at  $T \approx 4.2\text{ K}$  and  $35\text{ K}$  at zero magnetic field  $I_{\text{coil}} = 0$ .

We observe that with increasing temperature, the critical current ( $I_c$ ) decreases while thermal noise increases ( $I_{\text{th}} = \frac{2\pi k_B T}{\Phi_0} \approx 1.4\text{ }\mu\text{A}$ ). Consequently, as we approach temperatures in the range of 30-40K, we reach to the point where thermal noise becomes comparable to the Josephson energy and the critical current. At this stage, we expect by applying the optimum magnetic field across the device would result in the smaller critical current where it does not cross the origin due to rounding around  $I_c$ , which can be characterized by the noise parameter  $\Gamma = \frac{2\pi k_B T}{\Phi_0 I_0} = \frac{I_{\text{th}}}{I_c}$ . In the fig. 4.21, upon zooming in, we confirm that the critical current of the blue curve  $I_c \approx 2\text{ }\mu\text{A}$  and indeed it does not cross the origin as expected. Thus, the fact that it does not cross zero indicates that, the thermal energy rectified a certain small amount of voltage.

However as a physicist, we must always double-check our experimental setup. In this particular case, the lack of crossing origin may potentially be attributed to the shift of current source. To investigate whether this absence of crossing origin is indeed

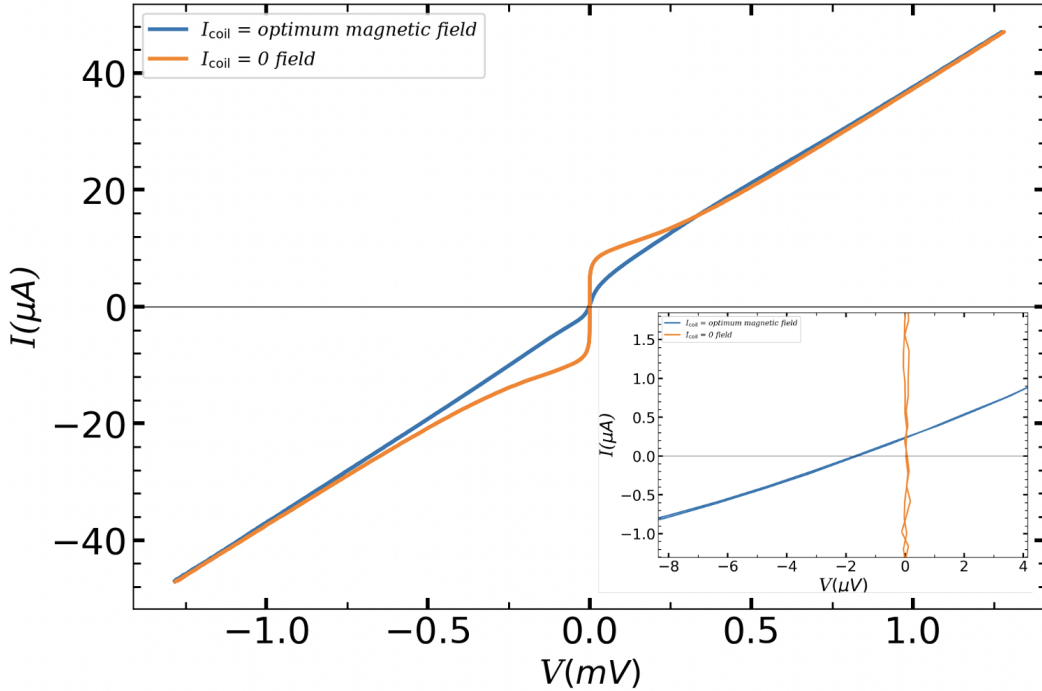


Figure 4.21: IVC for the ratchet A15 at around temperature 35K for the two values of  $I_{\text{coil}}$ : zero and the optimum magnetic field.

caused by the current source shift, we disconnect the cable from the current source and perform an additional measurement, as depicted in fig. 4.22.

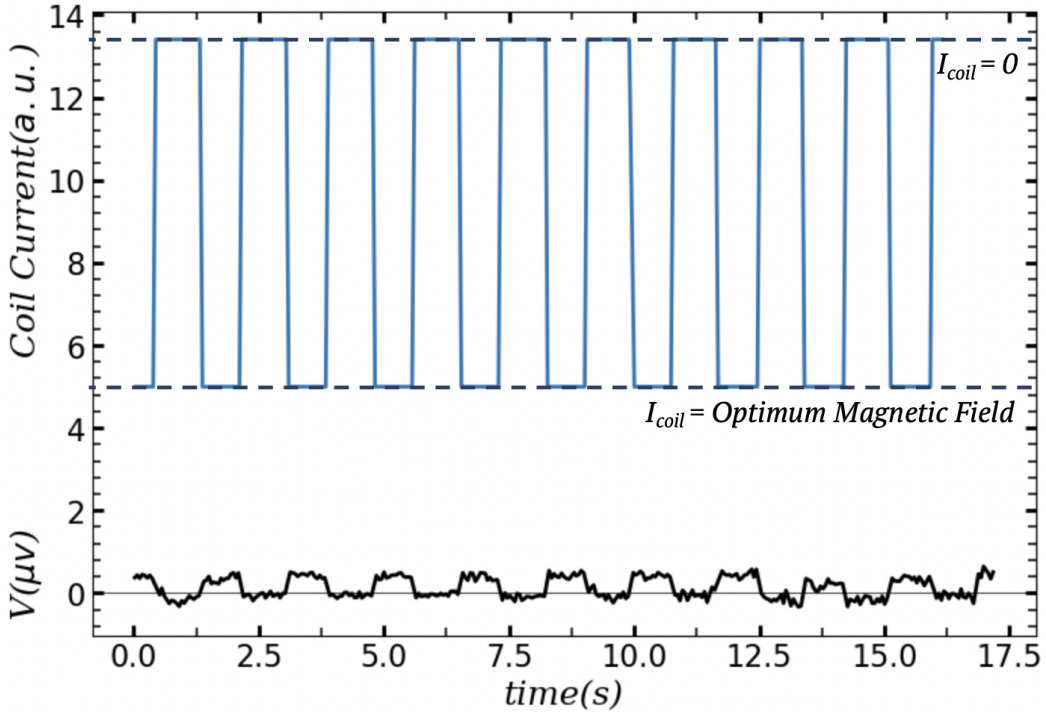


Figure 4.22

In this measurement, we recorded the voltage-versus-time  $V(t)$  data across our device A15 for two cases: when the coil current  $I_{\text{coil}}$  was set to 0 and when it was set to the optimum magnetic field. It was observed that when  $I_{\text{coil}} = 0$ , there was no voltage response, whereas for the optimum magnetic field, a voltage of approximately  $0.4 \mu\text{V}$  was observed. This voltage can be attributed to the rectification effect caused by the thermal noise. Based on these findings, we can conclude that the absence of zero-crossing in the blue curve depicted in fig. 4.21 is not due to a current shift but rather a result of thermal noises.

## 4.5 Conclusion

Utilizing He-FIB, we successfully operated the Josephson ratchets with an efficiency exceeding 75% with asymmetry parameter  $\mathcal{A} \approx 7$  and an average rectified dc voltage of approximately  $215 \mu\text{V}$ . We conducted experimental drives of the ratchet

in both deterministic and stochastic regimes, e.g. when the system operated with noises, capturing figures of merit along with corresponding experimental data for all ratchet parameters were given.

# References

- [1] P. Reimann, “Brownian motors: noisy transport far from equilibrium,” pp. 57–265, apr 2002. [Online]. Available: <https://doi.org/10.1016%2Fs0370-1573%2801%2900081-3>
- [2] M. Knufinke, K. Ilin, M. Siegel, D. Koelle, R. Kleiner, and E. Goldobin, “Deterministic josephson vortex ratchet with a load,” jan 2012. [Online]. Available: <https://doi.org/10.1103%2Fphysreve.85.011122>
- [3] E. Goldobin, R. Menditto, D. Koelle, and R. Kleiner, “Model I–V curves and figures of merit of underdamped deterministic josephson ratchets,” Sep 2016. [Online]. Available: <https://doi.org/10.1103%2Fphysreve.94.032203>
- [4] “Josephson effect,” [https://en.wikipedia.org/wiki/Josephson\\_effect](https://en.wikipedia.org/wiki/Josephson_effect).
- [5] R. Tumulka, “Foundations of quantum mechanics,” Nov 2022. [Online]. Available: <https://link.springer.com/book/10.1007/978-3-031-09548-1>
- [6] A. Barone, “Physics and applications of josephson effect,” 1982.
- [7] D. Kölle, “Basic properties of josephson junctions,” [https://nanocohybri.eu/wp-content/uploads/2019/01/Koelle\\_1.pdf](https://nanocohybri.eu/wp-content/uploads/2019/01/Koelle_1.pdf).
- [8] J. Roderiguez, “Characterization of josephson junctions created by he+ irradiation in commercial ceraco  $\text{YBa}_2\text{Cu}_3\text{O}_7 - x$  thin films,” p. Bachelor thesis, 2022. [Online]. Available: <https://doi.org/10.1016%2Fs0370-1573%2801%2900081-3>

- [9] B. Müller, M. Karrer, F. Limberger, M. Becker, B. Schröppel, C. Burkhardt, R. Kleiner, E. Goldobin, and D. Koelle, “Josephson junctions and SQUIDs created by focused helium-ion-beam irradiation of  $\text{YBa}_2\text{Cu}_3\text{O}_7$ ,” apr 2019. [Online]. Available: <https://doi.org/10.1103%2Fphysrevapplied.11.044082>